2011

Fabrication and Catalytic Property of Cerium Oxide Nanomaterials

Keren Jiang
University of Nebraska-Lincoln, kjiang@huskers.unl.edu

FABRICATION AND CATALYTIC PROPERTY OF CERIUM OXIDE NANOMATERIALS

By

Keren Jiang

A THESIS

Presented to the Faculty of

The Graduate College at the University of Nebraska

In Partial Fulfillment of the Requirements

For the Degree of Master of Science

Major: Chemistry

Under the Supervision of Professor Chin Li Cheung

Lincoln, Nebraska

June 2011

Fabrication and Catalytic Property of Cerium Oxide Nanomaterials

Keren Jiang, MS

University of Nebraska, 2011

Advisor: Chin Li Cheung

Cerium oxide, or ceria (CeO_x: x = 1.5 to 2), has been widely used as a heterogeneous catalyst. Ceria has several properties make it high catalytic active: the fluctuating valence of cerium, the high oxygen storage capacity and high oxygen mobility in the nonstoichiometric ceria. With the high abundance of cerium on earth crust, ceria is a highly effective alternative of the noble metal catalysts. Research has been focused on designing nanostructured ceria and ceria related materials in recent years. The catalytic activity of ceria can be enhanced by the nanoscale effect which can be applied for various designs of catalysts with unique properties.

In this thesis, I report two types of ceria-based nanomaterials fabricated by the electrochemical and dispersion-precipitation methods and our study of their physical and chemical properties. First, I discuss the fabrication of a ceria nanoporous membrane using a two-step method of anodization and subsequent calcination. A proposed anodization model involving the oxygen bubbles generation during the process for the growth of the nanoporous membranes is discussed. Second, I illustrate a new type of ceria-titania hybrid nanocomposites for oxidative catalysis. A dispersion-precipitation synthetic method for these catalysts and the evaluation of their oxidative catalytic activity are presented. Finally, I discuss other potential synthetic methods to produce and further enhance the catalytic activity of these hybrid nanocomposite catalysts.

Table of Contents

List of Figures

Acknowledgements

First, I would like to acknowledge my supervisor Dr. Chin Li Cheung. His support and guidance lead me to not only new scientific discoveries but also the way of thinking and solving problems as a scientist. I would like to thank Dr. Wonyoung Choe and Dr. Xiao Cheng Zeng for their help and advice in my research. I would also like to acknowledge my lab mates, especially Gonghua Wang and Neil J. Lawrence, for their help and support in my research and my life which made my time in and out the lab full of joy. Dr. You Zhou and Dr. Han Chen of the University of Nebraska-Lincoln Morrison Microscopy Core Research Facility provide me electron microscopy and were always helpful and willing to discuss the results of my experiments. I acknowledge Dr. Shah Valloppilly and Nebraska Center for Materials and Nanoscience for the help in X-ray diffraction. Finally, I want to thank Department of Chemistry and University of Nebraska-Lincoln providing me the opportunity to do my research.

Chapter 1 Introduction

Energy shortage and environmental pollution are two crucial challenges the world is facing. In order to solve these problems, new sources of energy and new technology of environmental protection methods are required. New materials could help in developing new energy source and treat the pollutions. Metal oxide materials with high catalytic activity and relatively low cost have becoming more popular in research and applications. [1-5] Thanks to the breakthroughs in atomic scales measurements and computational simulation, it is now possible to design and develop catalysts for specific target reactants and products. [6-10] Also, such breakthroughs allow the development of better methodologies to understand the principles and mechanisms behind the catalytic processes for metal oxides.

1.1 Cerium Oxide

The fifteen lanthanides together with scandium (Sc) and yttrium (Y) are called the rare earth metals. Among all the rare earths, cerium (Ce) is the most attractive one to researchers in the field of catalysis. Cerium is the most abundant rare earth element, making up about 0.0046% of the Earth's crust by weight (64 ppm), even more abundant than copper (60 ppm). [11, 12] It is found in a number of minerals, the most important being monazite and bastnasite. The high abundance, with its outstanding catalytic activity is one of the reasons leading cerium the element applied in catalytic exhaust conversion system of automobiles in industry. [13-15]

Cerium has four valence electrons $4f^2 6s^2$. [16, 17] It has two common oxidation states Ce(III) and Ce(IV). Cerium has 30 isotopes with atomic weights ranging from 123 to 152 g/mol. There are three stable isotopes: ^{136}Ce, ^{138}Ce and ^{140}Ce. The most abundant isotope is ^{140}Ce at 88.5%. [17] Cerium resembles iron in color and luster, but it is soft, malleable and ductile. Cerium has the second-longest liquid range of any element: 2648 °C (795 °C to 3443 °C). It oxidizes easily in air and burns readily at 150 °C to form cerium (IV) oxide. Cerium metal is commonly used in the ferro cerium fired steel metal alloy which applies in lighter flints. Metallic cerium is also added in micro-quantities to various alloys as an oxygen scavenger. The addition of cerium to the alloys can confer a longer operation life because of the improvement of their oxidative resistance.

Fluorite-structured cerium oxide (CeO_x: x = 1.5 to 2), or ceria, is produced by various methods according to different desired properties of the products. For bulk materials, to be used without purification, the oxide is collected during the refining process after adding the oxalate to nitric acid. For other materials, different precursors are used with a variety of synthetic methods. Methods for nanostructured ceria synthesis includes precipitation, milling, hydrothermal, sol-gel and surfactant assisted synthesis. For the synthesis of nanostructured ceria, common cerium precursors include cerium sulfate [$Ce_2(SO_4)_3$], cerium nitrate [$Ce(NO_3)_3$], ammonium cerium nitrate [$NH_4Ce(NO_3)_4$] and cerium chloride ($CeCl_3$). Cerium hydroxide is an important intermediate in many solvothermal and hydrothermal synthesis of cerium oxide nanomaterials.

One traditional application of ceria is in the glass industry as an efficient polishing agent for most glass compositions and also to prevent the decolorization of glass. These applications still consume a large portion of the cerium oxide products

produced. The addition of cerium (IV) oxide to the glass melt helps to convert iron to the low visible absorption ion, iron (II). The photostability of pigments is also enhanced by the addition of cerium as it provides the pigments with color fastness and prevents clear polymers from changing their color and thus blocking the solar light. Cerium oxide enhances the photostability of the polymer and pigments because its low absorption in the visible light and high absorption in the UV range. This protects the pigments used in glass coloration from the damage induced is by UV light exposure.

As much as forty percent by weight of the catalyst used for cracking crude oil in refinery operations is cerium and other rare earths. [18] Cerium also has minor uses in other commercial catalysis, such as the production of styrene from ethyl benzene, catalyzed by mixed iron and cerium oxide. [14, 18] Self-cleaning ovens utilize cerium oxide for its self-cleaning properties. The ceria is embedded in the walls and bottom of the oven and acts as an oxidative catalyst when the oven is heated. Cerium oxide is being increasingly used to clean vehicle exhaust streams through direct addition to diesel fuels to reduce sulfur emissions. [17-20]

1.2 Comparison of Materials' Properties: Bulk vs. Nanomaterials

R. Feynman stated that it would soon be possible to "arrange atoms the way we want" in 1959. [21] This talk was considered leading the breakthroughs of nanotechnology revolution. In the following 50 years, nanoscale materials have entered our daily lives and brought us huge benefits because of their size effect and their unique physical and chemical properties. Since nanomaterials differ so much from the bulk of

the same chemical composition in physical and chemical properties, they have become a field of study on their own.

Size effect, due to the surface to volume ratio of nanoscale materials, is one of the most important factors for the difference between the nanomaterials and the bulk. [22-25] By adopting nanoscaled structures, materials would increase their surface area dramatically. Also, the surface atoms of the nanomaterial are usually with higher reactivity due to unusual surface atomic re-arrangements. Surface atoms possess fewer nearest neighbors and therefore have dangling bonds exposed on the surface. Due to these dangling bonds, they are under an inwardly directed force that leads to the shortening of the bond distances between the surface atoms and the bulk atoms below. This bond shortening becomes more significant as the ratio of surface atoms to interior atoms increases. This extra energy possessed by the surface atoms leads to new properties including morphology, band gap, reactivity, and catalytic potential arrangements. [1, 2, 8, 14, 25-27]

1.3 Oxidation Catalysis

Since F. Haber discovered that the iron catalyst could increase the production rate of ammonia from nitrogen and hydrogen gases, the research of heterogeneous catalyst has been very active. It is estimated that more than 90% of industrial manufacturing processes worldwide utilize catalysis in one form or another. [27] According to the Food and Agriculture Organization of the United Nations, the worldwide demand for nitrogen-based fertilizer will be 111.6 million tons in 2014 at the annual growth of 1.8 percent. [28]

Virtually all nitrogen fertilizer is produced as ammonia utilizing the Haber-Bosch process, leading to this process being named the “invention of the century”. [27,29]

Catalysis provides a means to change the rates and control the yields of chemical reactions so as to increase the desirable products and reduce the amounts of undesirable ones. The reduced emissions of automobiles and the abundance of fresh food are made possible by chemical reactions controlled by catalysts. Catalysis is also essential in contributing to a healthy economy. The petroleum, chemical, and pharmaceutical industries, contributors of $500 billion to the gross national product of the United States, rely on catalysts to produce everything from fuels and “wonder drugs” to paints and cosmetics.

Catalysis is defined as a process which promotes an increase or decrease in the reaction rate but not the reaction equilibrium by adding extra chemical ingredients (catalysts) besides the reagents. When the reaction reaches equilibrium, the catalysts added maintain the same quantity and chemical composition. Heterogeneous catalysis involves at least one of the reactants being in a distinct phase from the catalyst. This thesis focuses on reactions in which the catalyst is in the solid phase and the reactants are either liquids or gases.

The mechanism of catalytic activity on ceria is a subject under exploring. The cited reasons tend to revolve around their high oxygen storage capacity (OSC) which is largely due to the multivalent nature of cerium and the high mobility of the oxygen vacancies at the surface of the materials. The ability of heterogeneous cerium oxide catalysts to change in the activation energy for reactions is largely due to the surface effect. The shift between the Ce (III) to Ce (IV) states leads to a high oxygen mobility in

ceria lattice, which in turn can lead to its enhanced catalytic activity. Recently, the controlled synthesis of functional nanosized ceria has become popular. [10]

The high oxygen mobility in the ceria lattice can be attributed to the size, dispersion, and quantity of oxygen vacancy defects (OVD) in the lattice. Once sub-surface oxygen vacancy sites are introduced into the lattice, the mobility of the vacancies, and thus the defects, is greatly decreased. Vacancy clusters tend to form in the three or six surrounding cerium ions of the materials' surface. [4, 11, 30-34]

1.4 Thesis Overview

In this thesis, two types of synthetic methods of cerium oxide nanomaterials are presented. In Chapter 2, an anodization method for fabricating cerium oxide nanoporous membranes from cerium metal foil will be discussed. In Chapter 3, a novel hybrid ceria-titania nanocomposite and its catalytic activity towards carbon monoxide oxidation will be presented. Finally, future potential catalyst development from the insights obtained in Chapter 2 and 3 will be proposed in Chapter 4.

1.5 References

1. Campbell, C.T., *Ultrathin metal films and particles on oxide surfaces: structural, electronic and chemisorptive properties.* Surface Science Reports, 1997. **27**(1-3): p. 1-111.
2. Castellani, N.J., Branda, M.M., Neyman, K.M. and Illas, F., *Density Functional Theory Study of the Adsorption of Au Atom on Cerium Oxide: Effect of Low-Coordinated Surface Sites.* Journal of Physical Chemistry C, 2009. **113**(12): p. 4948-4954.
3. Trovarelli, A., *Catalysis by Ceria and Related Materials*. Catalytic Science Series, ed. G.J. Hutchings. Vol. 2. 2002, London: Imperila College Press. 508.
4. Nolan, M., Parker, S.C., and Watson, G.W., *CeO_2 catalysed conversion of CO, NO_2 and NO from first principles energetics.* Physical Chemistry Chemical Physics, 2006. **8**(2): p. 216-218.
5. Ong, K.G., Varghese, O.K., Mor, G.K., Shankar, K. and Grimes, C.A., *Application of finite-difference time domain to dye-sensitized solar cells: The effect of nanotube-array negative electrode dimensions on light absorption.* Solar Energy Materials and Solar Cells, 2007. **91**(4): p. 250-257.
6. Bartholomew, C.H. and Farrauto, R.J., *Fundamentals of industrial catalytic processes*. 2nd ed. 2006, Hoboken, N.J.: Wiley. xxiii, 966 p.
7. Boudart, M., *Turnover Rates in Heterogeneous Catalysis.* Chemical Reviews, 1995. **95**(3): p. 661-666.

8. Campbell, C.T., *Metal films and particles on oxide surfaces: Structural, electronic and chemisorptive properties.* Journal of the Chemical Society-Faraday Transactions, 1996. **92**(9): p. 1435-1445.

9. Feng, X.J., Shankar, K., Varghese, O.K., Paulose, M., Latempa, T.J., and Grimes, C.A., *Vertically Aligned Single Crystal TiO_2 Nanowire Arrays Grown Directly on Transparent Conducting Oxide Coated Glass: Synthesis Details and Applications.* Nano Letters, 2008. **8**(11): p. 3781-3786.

10. Fornasiero, P., Dimonte R., Rao G. R., Kaspar J., Meriani S., Trovarelli A. and Graziani M., *Rh-Loaded CeO_2-ZrO_2 Solid-Solutions as Highly Efficient Oxygen Exchangers: Dependence of the Reduction Behavior and the Oxygen Storage Capacity on the Structural-Properties.* Journal of Catalysis, 1995. **151**(1): p. 168-177.

11. Ganduglia-Pirovano, M.V., A. Hofmann, and J. Sauer, *Oxygen vacancies in transition metal and rare earth oxides: Current state of understanding and remaining challenges.* Surface Science Reports, 2007. **62**(6): p. 219-270.

12. Ivanova, A.S., *Physicochemical and Catalytic Properties of Systems Based on CeO_2.* Kinetics and Catalysis, 2009. **50**(6): p. 797-815.

13. Nolan, M., S.C. Parker, and G.W. Watson, *Reduction of NO_2 on ceria surfaces.* Journal of Physical Chemistry B, 2006. **110**(5): p. 2256-2262.

14. Nolan, M. and G.W. Watson, *The surface dependence of CO adsorption on ceria.* Journal of Physical Chemistry B, 2006. **110**(33): p. 16600-16606.

15. Pirmohamed, T., Dowding J.M., Singh S., Wasserman B., Heckert E., Karakoti A.S., King J.E., Seal S., Self W.T., *Nanoceria exhibit redox state-dependent catalase mimetic activity.* Chemical Communications, 2010. **46**(16): p. 2736-2738.

16. Deshpande, S., Patil, S., Kuchibhatla, S. VNT., Seal, S., *Size dependency variation in lattice parameter and valency states in nanocrystalline cerium oxide.* Applied Physics Letters, 2005. **87**(13): p. 3.

17. Hedrick, J.B., *Rare Earths*. U.S. Geological Survey Minerals Yearbook-2001, 2001. **61**: p. 1-17

18. Conesa, J.C., Martinez-Arias, A., Fernandez-Garcia, M., and Soria, J., *Surface structure and redox chemistry of ceria-containing automotive catalytic systems.* Research on Chemical Intermediates, 2000. **26**(1): p. 103-111.

19. Kim, C.H., Qi, G. Dahlberg, K. and Li, W., *Strontium-Doped Perovskites Rival Platinum Catalysts for Treating NO_x in Simulated Diesel Exhaust.* Science, 2010. **327**(5973): p. 1624-1627.

20. Nolan, M., Parker, S.C., and Watson, G.W., *The electronic structure of oxygen vacancy defects at the low index surfaces of ceria.* Surface Science, 2005. **595**(1-3): p. 223-232.

21. Feynman, R. P., and Sykes, C., *No ordinary genius: the illustrted Richard Feynman*, 1995, New York: W. W. Norton & Company, Inc. 175.

22. Caps, V., Arrii, S., Morfin, F., Bergeret, G., and Rousset, J., *Structures and associated catalytic properties of well-defined nanoparticles produced by laser vaporisation of alloy rods.* Faraday Discussions, 2008. **138**: p. 241-256.

23. Park, J., Bauer, S., von der Mark, K., and Schmuki, P., *Nanosize and vitality: TiO_2 nanotube diameter directs cell fate.* Nano Letters, 2007. **7**(6): p. 1686-1691.

24. Prakasam, H.E., Varghese, O.K., Paulose, M., Mor, G.K. and Grimes, C.A., *Synthesis and photoelectrochemical properties of nanoporous iron (III) oxide by potentiostatic anodization.* Nanotechnology, 2006. **17**(17): p. 4285-4291.

25. Wang, W.Z., Varghese, O.K., Paulose, M., Grimes, C.A., Wang, Q., and Dickey, E.C., *A study on the growth and structure of titania nanotubes.* Journal of Materials Research, 2004. **19**(2): p. 417-422.

26. Branda, M.M., Hernandez, N.C. Sanz, J.F., and Illas, F., *Density Functional Theory Study of the Interaction of Cu, Ag, and Au Atoms with the Regular CeO_2 (111) Surface.* Journal of Physical Chemistry C, 2010. **114**(4): p. 1934-1941.

27. Masel, R.I., *Chemical Kinetics and Catalysis*, 2001, Wiley-Interscience, New York, p. 10.

28. *Current world fertilizer trends and outlook to 2014*, Food and Agriculture Organization of the United Nations, Rome, 2010.

29. Sittig, M., *Fertilizer Industry: Processes, Pollution Control and Energy Conservation*, 1979, New Jersey: Noyes Data Corp.

30. Nolan, M., Verdugo, V.S., and Metiu, H., *Vacancy formation and CO adsorption on gold-doped ceria surfaces.* Surface Science, 2008. **602**(16): p. 2734-2742.

31. Babu, S., Thanneeru, R., Inerbaev, T., Day, R., Masunov, A.E., Schulte, A., and Seal, S., *Dopant-mediated oxygen vacancy tuning in ceria nanoparticles.* Nanotechnology, 2009. **20**(8).

32. Dholabhai, P.P., Adams, J.B., Crozier, P., and Sharma, R., *Oxygen vacancy migration in ceria and Pr-doped ceria: A DFT plus U study.* Journal of Chemical Physics, 2010. **132**(9): p. 094104.

33. Liu, X., Zhou, K., Wang, L., Wang, B., and Li, Y., *Oxygen Vacancy Clusters Promoting Reducibility and Activity of Ceria Nanorods.* Journal of the American Chemical Society, 2009. **131**(9): p. 3140-3141.

34. Nolan, M., *Molecular Adsorption on the Doped (110) Ceria Surface.* Journal of Physical Chemistry C, 2009. **113**(6): p. 2425-2432.

Chapter 2 Porous Cerium Oxide Membrane

2.1 Introduction

Metal oxide membrane has been produced from anodization method for over 80 years. However, forming a membrane with exfoliating oxides has been a problem for a long time. This kind of membrane can be used in a variety of catalytic applications. One of the most current applications is the electrolyte in solid fuel cells. [1, 2]

Solid oxide fuel cells (SOFC, Figure 2.1) are attracting a lot of research interests because of their promising future in large-scale power application such as centralized electricity generation and mobile power plants. With an operating temperature around 1000 °C, SOFC could generate a large amount of electric power by converting natural gas into water and carbon dioxide. Theoretically, the SOFC membrane should have certain characteristics: 1) It should efficiently catalyze the reactions in the SOFC; 2) It should be hydrophobic to avoid water poisoning itself; and 3) The membrane should be electrically conductive. SOFC membranes made of cerium oxide cause most of the interest due to their rich oxygen content, semi conductivity and also the catalytic ability. [1-4]

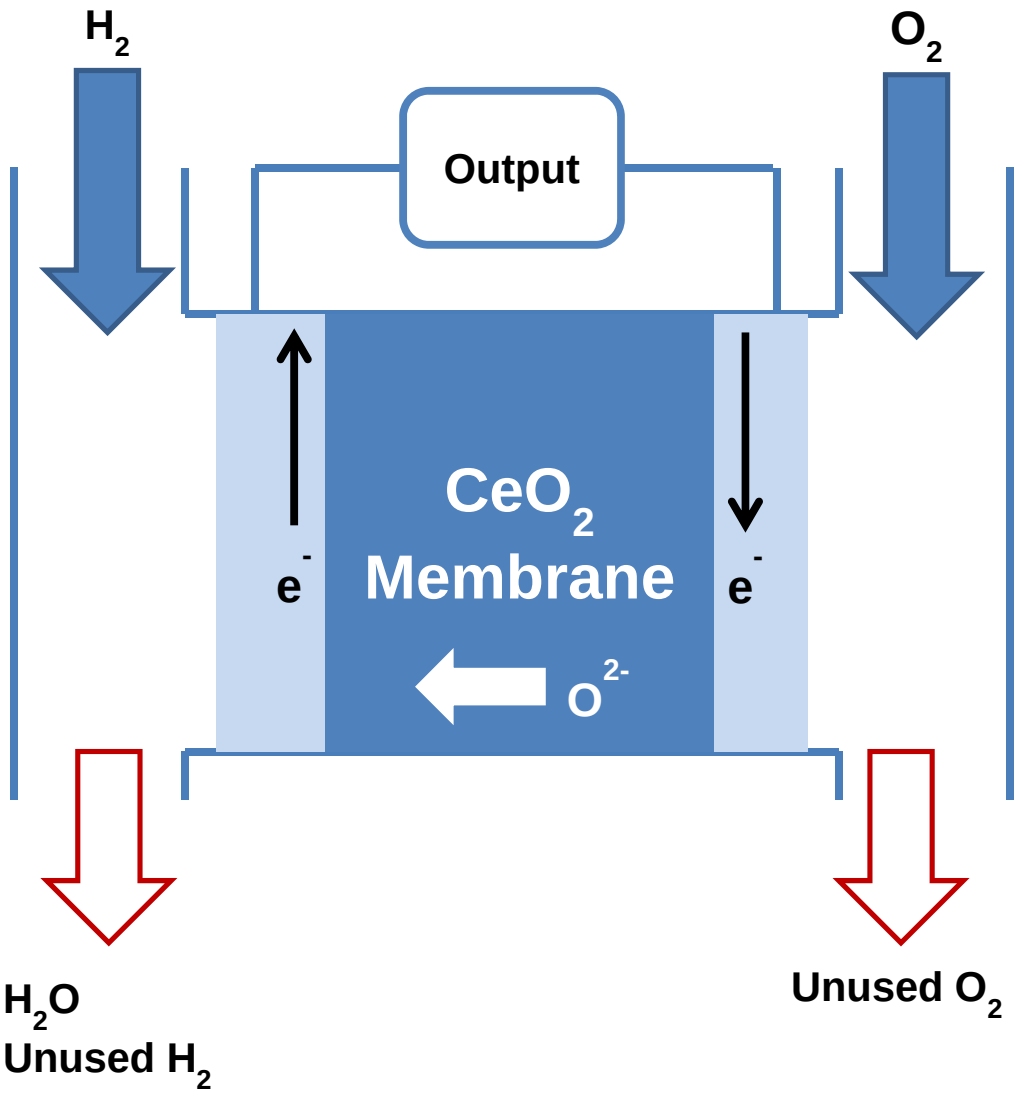

Figure 2.1 Schematic of a solid oxide fuel cell (SOFC).

However, there are two major disadvantages of utilizing cerium oxide as the electrolyte in SOFC. The first one is the cerium oxide's high dielectric property which makes it inefficient in transporting electrons. This was proposed to be solved by doping or decorating other conductive material such as samarium to increase its conductivity. The other problem is that the cerium oxide is an exfoliating oxide. The demand to make a membrane that does not exfoliate will be discussed in this chapter.

Fabrication of a membrane of exfoliating oxide is difficult. Since 1920's, anodization has been commonly used to synthesize various kinds of oxide films on metal surfaces. Anodized aluminum, for example, is a commonly used protective layer in industry. [5, 6] In recent 20 years, anodization of metal foil has been applied to synthesize oxide membranes with nanostructures. However, anodization of metals whose oxides exfoliate has been a problem. The two existing models of anodization are the aluminum model in which the metal foil is directly anodized to the oxide, and the zinc model in which the foil is anodized to the sulfate or phosphate. [7, 8]

In this chapter, a new anodization model is proposed. In this model, the cerium metal is anodized to an inorganic polymer in the form of cerium hydroxide. The adhesion of the membrane formed on the metal surface enables the anodization to continue to convert the whole foil in to the hydroxide. A followed calcination step is then applied to convert the cerium hydroxide polymer membrane to cerium oxide. This strategy has the potential leading to a large scale anodization process and applications in the fields of protective coating and the oxide membranes fabrication.

2.2 Synthetic Method

Cerium metal foil was first cut into 1 cm x 1cm squares and polished with 1-μm diamond grit until a mirror-like finish was achieved. The samples were sonicated in acetone for 15 minutes to remove any remaining diamond grit particles, and then dried with nitrogen. The dry samples were anodized in a two-electrode cell with the cerium foil as the anode and a 1 cm × 1 cm platinum foil as the cathode. To prevent the alligator clips holding the cerium anode from contacting the electrolyte, a piece of bent w-shaped platinum (Pt) foil was used to protect the cerium metal foil. The electrolyte solution was composed of ethylene glycol, ammonium hydroxide and water in ratios adjusted for each set of experimental conditions. The anodization was accomplished by applying a constant current of 100 μA with a source meter (Keithley 2410, Keithley Instruments Inc. Cleveland, OH) for 160 h. The membrane was considered to be fully anodized once the applied potential at 100 μA reached the limit of the source meter (1000 V). The membrane was then rinsed thoroughly with ethanol, dried under a nitrogen stream and immersed in a 100 mL ethanol bath for 12 h. The ethanol bath was gently stirred to facilitate the removal of remaining traces of electrolyte from the membrane structures. Afterwards, the sample was dried in a gentle stream of dry nitrogen. Conversion of the as-anodized membrane samples into cerium (IV) oxide was achieved by calcination at 400 °C for 2 h. under a flow of 100 SCCM dry air inside a 1" quartz tube vacuum furnace at 0.12 Torr. The temperature of the furnace was increased at a rate of 0.5 °C/min. so as to control the calcination rate of the structures and to promote gentle evaporation of any remaining solvent.

2.3 Membrane Characterization: Materials Structures, Chemical Composition, and Water Wettability

The morphology of the processed samples was investigated by field emission scanning electron microscopy (FE-SEM, Hitachi S4700, Hitachi High Technologies America, Inc., Pleasanton, CA). The crystal structures of the samples were studied by Rigaku D/Max-B diffractometer equipped with Cu K_α X-ray source of average wavelength 1.544 Å (Rigaku America, The Woodlands, TX). Confocal Raman microscopy on the samples was performed with a HR800 confocal Raman microscope (Horiba Scientific, Kyoto Japan, LabRAM) using a 20 mW 632.8 nm He-Ne laser. Water contact angle measurements on the samples were performed using 0.25-μL droplets of ultrapure water with the video contact angle analysis equipment (VCA Optima, AST Products, Inc., Billerica, MA). The AST software was used for the contact angle measurements in the recorded optical images.

Typical scanning electron microscopy (SEM) images of the anodized cerium foil calcined at 400 °C revealed the "ribbon-like" structures forming the backbones of the porous frame work (Figure 2.2a and 2.2b). The average thickness of these "ribbon-like" structures was 24 $\pm$ 4 nm. Full anodization of a foil sample was usually found to be split it into two membranes of $\approx$125 μm in thickness. Side view SEM images of these membranes indicated that these membranes were composed of channels of pores formed perpendicular to the membrane surface. Transmission electron microscopy (TEM) image and a selected area electron diffraction pattern of one "ribbon-like" structure suggested that the sample calcined at 400 °C is made of highly crystalline ceria (Figure 2.2c).

Zoomed-in TEM image (Figure 2.2d) of the structure showed a lattice fringe pattern with spacing of 0.31 nm which corresponded to those of ceria (111) facets.

The crystal structures of the anodized cerium foil and their transformation by calcination were characterized by X-ray diffraction (XRD) (Figure 2.3) and indexed against JCPDS data. The XRD pattern of a fully anodized cerium foil suggested that the anodization process transformed the cerium metal foil into $P6_3/m$ hexagonal cerium (III) hydroxide [$Ce(OH)_3$] and hexagonal Ce_2O_3. The pattern also indicated the presence of a trace amount of α-Ce metal which implies that some cerium metal may be preserved between the pores. Small deposits of metal were likely located in areas where the hydroxide thickness of the pores limits the oxidation at the applied potential. The XRD patterns of anodized samples calcined at 50, 275 and 400 ˚C were also collected to verify the transformation of the anodized samples into cubic ceria. Compared to the XRD pattern of the as-anodized sample, the relative intensities of diffraction peaks belonging to the cerium hydroxide and metal in the XRD pattern of the sample calcined at 50 ˚C decrease significantly. For samples calcined at higher temperatures, diffraction peaks of the fluorite structure were dominant in the corresponding XRD patterns. There were no indications of metallic cerium in these patterns. Only the XRD pattern of the sample calcined at 400 ˚C showed no satellite peaks belonging to $Ce(OH)_3$ and hexagonal Ce_2O_3, indicating a complete conversion of the sample into fluorite ceria.

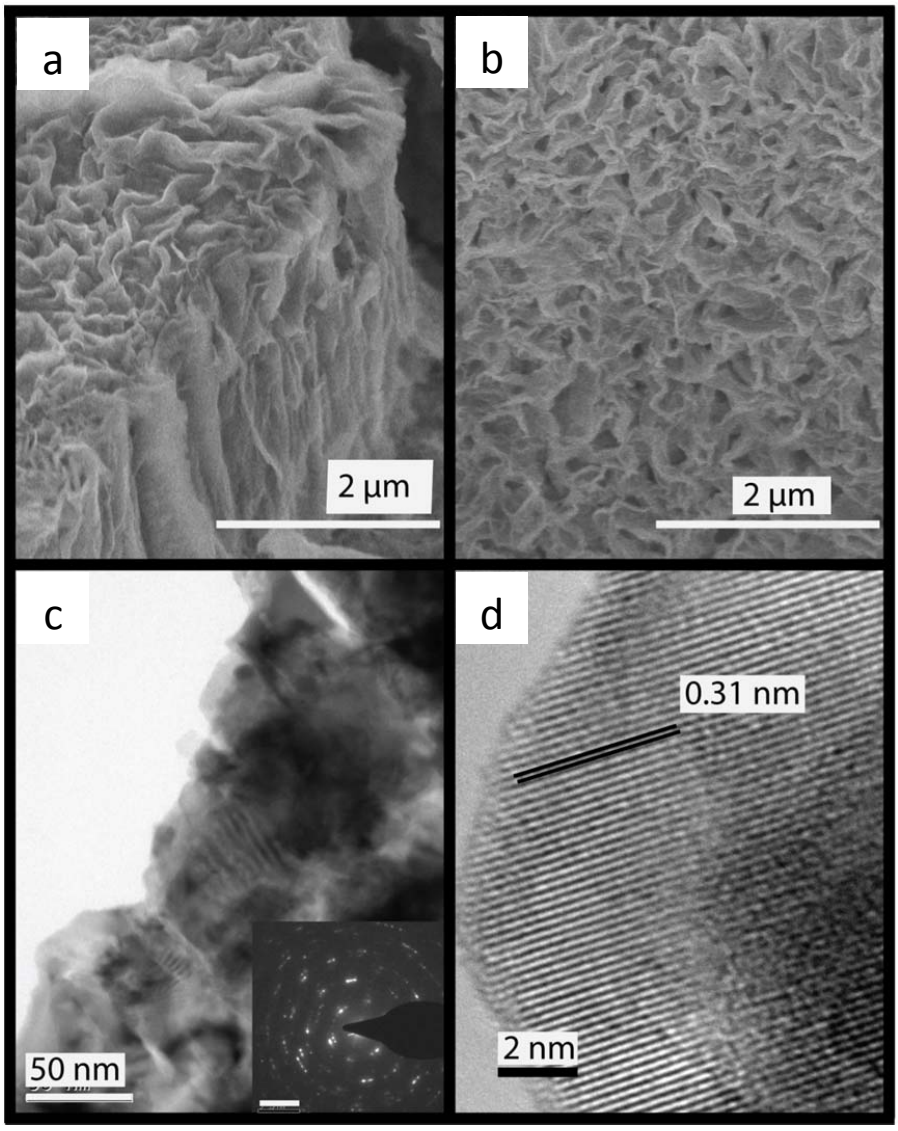

Figure 2.2 Ceria porous membranes made by a two-step anodization-calcination process. (a) Oblique view and (b) top view SEM images illustrate the porous nature of membrane and "ribbons-like" frameworks on the membrane surface. (c) TEM image of a ribbon structure. (inset) SAED pattern. (d) HRTEM image of one piece of the "ribbon-like" framework. The lattice plane spacing is consistent with those of ceria (111) facets.

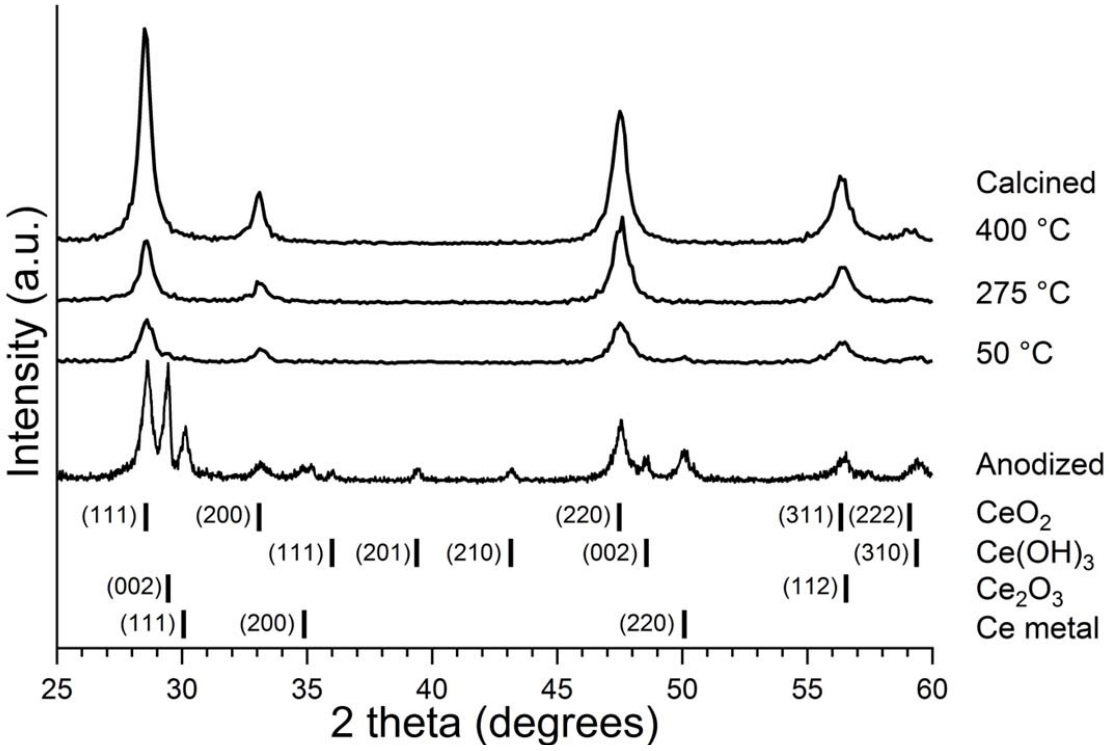

Figure 2.3 XRD patterns showing the transition of as-anodized cerium foils from simple hexagonal cerium (III) hydroxide ($Ce(OH)_3$) to fluorite-structured ceria (CeO_x) as the calcination temperature increases 50, 275 to 400 ˚C. (Bottom) Vertical lines showing peak indexes of CeO_2, $Ce(OH)_3$, Ce_2O_3 and α-Ce from the corresponding JCPDS data.

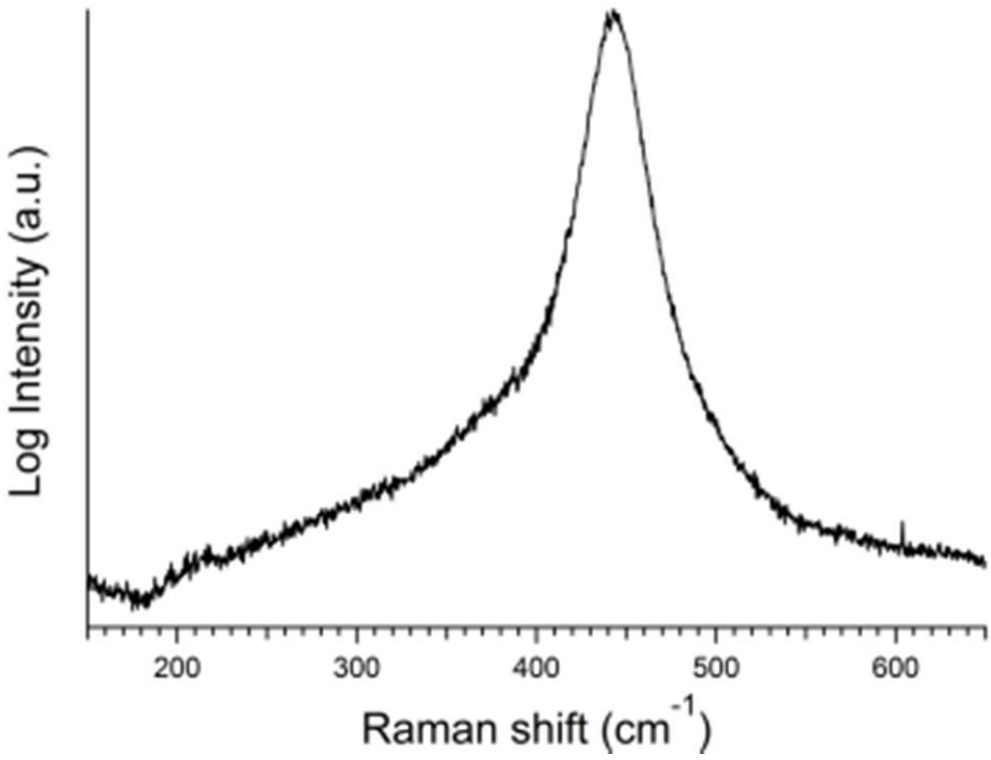

Figure 2.4 Raman scattering spectrum of an anodized ceria membrane calcined at 400 ˚C.

Raman scattering spectrum (Figure 2.4) of the porous CeO_x membrane displayed a peak near 462 cm^{-1}, which was typically assigned to the T_{2g} mode of the Ce-O vibrational unit with O_h symmetry. No other significant peaks were found in this spectrum, indicating that the annealed membrane did not have a significant number of lattice related defects.

The effect of the porous structures on the water wettability of the ceria membrane was examined by water contact angle measurements (Figure 2.5). The apparent advancing water contact angles of 0.25 μl water droplets on the calcined CeO_x membranes were measured to be 120 ± 4°. Water contact angle measurements were also performed on calcined and samples with the porous structures destroyed by sonication in ethanol and on air-oxidized cerium foil. The corresponding measurements yield values of 31 ± 3° and 17 ± 3° respectively, suggesting the necessity of porous structures in the apparent hydrophobic nature of the ceria membranes. Cassie-Baxter model was applied to describe the apparent water contact angle (θ_c) of a textured hydrophobic surface:

$$\cos\theta_c = f_1 \cos\theta_1 + f_2 \cos\theta_2 \qquad (1)$$

where f_1 and f_2 are the surface area fractions of the membrane for components 1 and 2. The contact angles θ_1 and θ_2 are of water on a smooth surface of components 1 and 2. When the droplet is water and air is the trapped gas, θ_2 is 180°, allowing the re-expression of eqn. 1 as

$$\cos\theta_c = f_1(\cos\theta_1 + 1) - 1 \qquad (2)$$

Utilizing eqn. 2, the area fraction of the solid-water interface for the porous membrane surface f_1 was estimated to be ca. 0.62. Given that the surface was topographically irregular and it did not contain large changes in the chemical hydrophobicity, the Cassie-Baxter model was adequate to explain our measurements. This fraction correlates well to the average value estimated from SEM images of the membranes (0.51 ± 0.03).

The calculation of the surface area fractions from top view SEM images of the porous ceria membranes was accomplished using the NIH software package Image-J.1 For a typical top view SEM image of a porous ceria membrane (Figure 2.6a), the ridges between the pores are shown as the light shaded areas whereas the pores (cavities) are shown as the dark shaded areas. When a water droplet is dispensed on the porous membrane, the portion of surface area in contact with the water is composed of the ridges and upper portions of the pore structures. The Image-J software allows setting of a relative threshold brightness ratio between the structures with different shades in the SEM images (Figure 2.6b) and converts all the apparent pore area to appear as white and the rest as black. The process was automated using Image-J's built in scripting language as illustrated in Program 1 for our contact surface area estimation (See Appendix). Following the conversion of the image into white areas (non-contact pore) and black areas (possible water contact surface area), Image-J calculates and reports these two apparent surface areas. The mean surface area fraction which describes the fraction of apparent surface area possibly in contact with a water droplet is estimated to be 0.51 ± 0.03. Owing to the irregularity of the ceria membrane surface structures, this mean surface area fraction is likely to be underestimated using this apparent surface area estimation method. Nonetheless, visual inspection appears to match this estimated value.

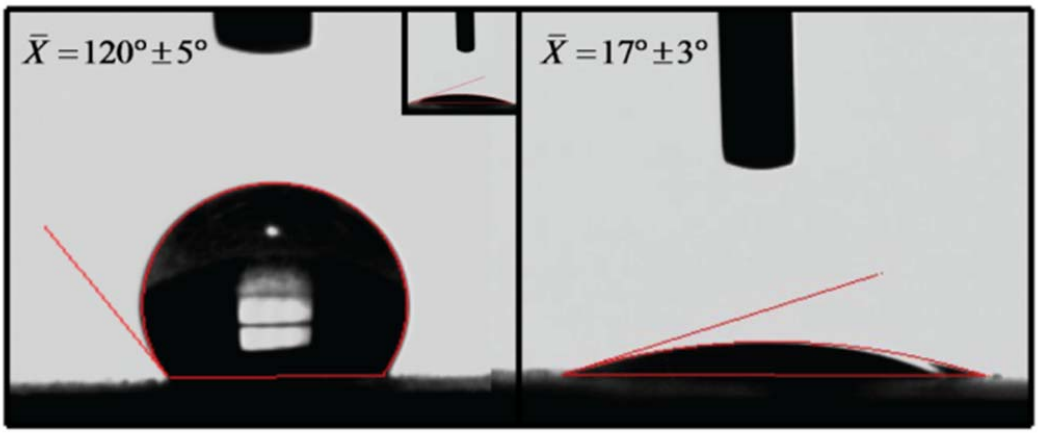

Figure 2.5 Optical images showing water contact angle measurements on (left) an anodized porous ceria membrane and (right) an cerium oxide surface formed on a piece of cerium metal oxidized under ambient conditions. (Inset) Water contact angle measurement on an anodized porous ceria membrane with its "ribbon-like" structures destroyed by sonication in ethanol. The measured water contact angle on this surface is 31 ± 3˚.

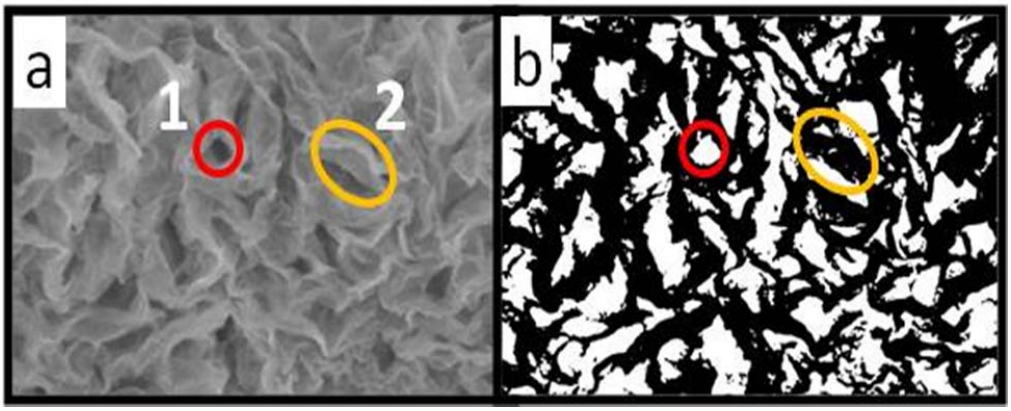

Figure 2.6 (a) Top view SEM image of ribbon-like nanostructures as imaged. Circle1 (red) is an example of a pore. Ellipsoid 2 (yellow) is a model ridge of the ribbon-like structures. (b) Processed SEM image with Image-J. The pores are represented by the white areas whereas the ridges between the pores are represented by the black areas.

2.4 Synthetic Mechanism

A multi-stage formation mechanism for the porous anodized cerium foil structures with "ribbon-like" backbone framework can be deduced from the experimental observations and possible electrochemical reaction scheme (Figure 2.7). In the initial stage of the anodization, cerium metal was electrochemically oxidized to cerium (III) ions (Ce^{3+}). At the metal surface, the formation of soluble complexes ($[Ce(NH_3)_{12-x}](OH)_x$) led to pitting of the metal foil surface. Electric fields enhanced by the high curvatures of the pits possibly caused an increase in the pit size. The Ce^{3+} ions reacted with hydroxide ions to form $Ce(OH)_3$ polymers. The $Ce(OH)_3$ likely to form $Ce\text{-}NH_3\text{-}H_2O$ complex which was soluble chemical species. The formation of this complex possibly caused the dissolution of the $Ce(OH)_3$.

An increase in the ammonia concentration of the electrolyte was found to produce a decrease in the density and thickness of the "ribbon-like" structures. The cerium anode simply appeared to dissolve into the electrolyte solution. This was likely caused by the increased formation rate of the soluble ammonia complexes which competed with the precipitation and formation of the cerium hydroxide framework. However, if the concentration of ammonium ions was very low or the ammonium ions were replaced by sodium ions, the cerium oxide was observed to form, and then exfoliate from the cerium foil. Therefore, the concentration of NH_4^+ ions is critical to the proper formation of the membrane.

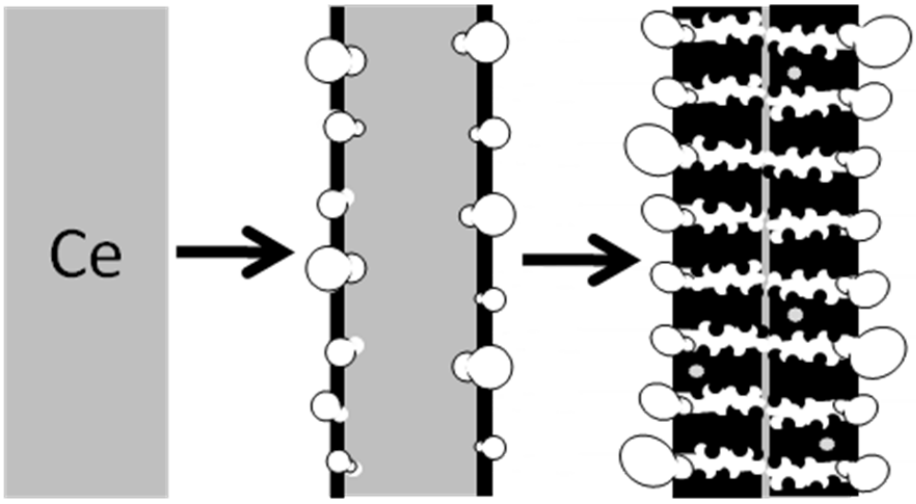

Figure 2.7 Proposed mechanism for the formation of the porous anodized structures from a cerium metal foil. Gray is cerium metal and black is the anodized complex. The cerium metal acts as the anode in the electrochemical cell. As a complex layer begins to form, vapor filled voids (cavities) or "bubbles" form on the surface and create pathways to the metal, allowing the diffusion of reactants to the metal surface. Pores are formed from volume changes due to the formation of the cerium hydroxide. The formation of gas cavities allow the reaction to continue to completion. Small deposits of metal may be left as shown in the final stage of the anodization.

At the surface of the cerium foil, oxygen was produced in the oxidation reaction and cavities (vapor filled bubbles) were observed trapped in the porous matrix during the anodization process. The radius (r) of a cavity before it left the surface of a solid is a function of the buoyancy of the trapped vapor (P_{in}) being resisted by the pressure of the liquid (P_{out}) and the surface tension (γ) causing the adhesion of the cavity to the solid. The use of an electrolyte with a surface tension much less than that of water favored the formation of smaller cavities as indicated by the Young-Laplace relationship.

$$r = \frac{2\gamma}{P_{in} - P_{out}} \qquad (3)$$

The formation of the low-solubility $Ce(OH)_3$ precipitated around the cavities, leading to the growth of the thin "ribbon-like" structures of the porous framework. As the cavities of trapped gas increased in size, they eventually escaped, leaving voids adjacent to bare metal and allowing the continuation of the anodization process.

Current density appears to affect the growth rate of the "ribbons-like" structures. At a fixed current, the thickness of the cerium hydroxide porous structures increased at a constant rate. An increase or decrease in applied current was found to change the film growth rate of growth proportionally. The pore size was observed to increase with an increase in current density. Similar to the case of anodizing porous silicon, once a threshold current level was reached, the pore diameters of the anodized structures became too large that a smooth surface was obtained instead.

2.5 Conclusion

A two-step synthetic strategy has been successfully demonstrated to fabricate porous membranes of cerium oxide that does not exfoliate. The reported strategy has the potential to lead to scientific and commercial progress in the fabrication of protective coatings and porous membranes made of oxides which would otherwise exfoliate. A new mechanism of the cerium anodization is proposed. It could lead to a variety of applications for creating exfoliating oxide membranes on metal surface.

2.6 Appendix

Program 1 – Calculate the area on nanoribbons

```
// "Calculate the area on Nanoribbons"
//
// This script will batch process the .tif images in a given folder and subfolders
// and will calculate the ratio of the area of the ribbon edges to the area of the pore.
// This is accomplished by converting the image to binary (black and white) and reporting
// the percentage of the area that is above the threshold for conversion to black.
// the threshold level can be set manually if the contrast of the original image is too low.
//
// This macro batch processes all the files in a folder and any
// subfolders in that folder.

  requires("1.33s");
  dir = getDirectory("Choose a Directory ");
  sav = getDirectory("Choose a Save Directory ");
  setBatchMode(true);
  count = 0;
  countFiles(dir);
  n = 0;
  processFiles(dir);
  print(count+" files processed");

  function countFiles(dir) {
    list = getFileList(dir);
    for (i=0; i<list.length; i++) {
        if (endsWith(list[i], "/"))
```

```
            countFiles(""+dir+list[i]);
        else
            count++;
    }
}
 function processFiles(dir) {
    list = getFileList(dir);
    for (i=0; i<list.length; i++) {
        if (endsWith(list[i], "/"))
            processFiles(""+dir+list[i]);
        else {
          showProgress(n++, count);
          path = dir+list[i];
          processFile(path);
        }
    }
}
 function processFile(path) {
     if (endsWith(path, ".tif")) {
//main function
       open(path);
                run("Make Binary");
                run("Analyze  Particles...",  "size=0-Infinity  circularity=0.00-1.00
show=Masks display clear summarize");
                done = sav+"done_"+list[i];
                saveAs("Tiff", done);
    }
}
```

2.7 References

1. Deluga, G.A., Salge, J.R., Schmidt, L.D., and Verykios, X.E., *Renewable hydrogen from ethanol by autothermal reforming.* Science, 2004. **303**(5660): p. 993-997.
2. Park, S.D., Vohs, J.M., and Gorte, R.J., *Direct oxidation of hydrocarbons in a solid-oxide fuel cell.* Nature, 2000. **404**(6775): p. 265-267.
3. Kim, C.H., Qi, G., Dahlerg, K., and Li, W., *Strontium-Doped Perovskites Rival Platinum Catalysts for Treating NO_x in Simulated Diesel Exhaust.* Science, 2010. **327**(5973): p. 1624-1627.
4. Murray, E.P., Tsai, T., and Barnett, S.A., *A direct-methane fuel cell with a ceria-based anode.* Nature, 1999. **400**(6745): p. 649-651.
5. Mor, G.K., Shankar, K., Paulose, M., Varghese, O.K., and Grimes, C.A., *Use of highly-ordered TiO_2 nanotube arrays in dye-sensitized solar cells.* Nano Letters, 2006. **6**(2): p. 215-218.
6. Varghese, O.K., Gong, D., Paulose, M., Grimes, C.A., and Dickey, E.C., *Crystallization and high-temperature structural stability of titanium oxide nanotube arrays.* Journal of Materials Research, 2003. **18**(1): p. 156-165.
7. Grimes, C.A., Ong, K.G., Varghese, O.K., Yang, X., Mro, G., Paulose, M., Dickey, E.C., Ruan, C., Pishko, M.V., Kendig, J.W. and Mason, A.J., *A sentinel sensor network for hydrogen sensing.* Sensors, 2003. **3**(3): p. 69-82.
8. Mor, G.K., Shankar, K., Varghese, O.K., and Grimes, C.A., *Photoelectrochemical properties of titania nanotubes.* Journal of Materials Research, 2004. **19**(10): p. 2989-2996.

Chapter 3 Synthesis and Catalytic Property of Hybrid CeO_x-TiO_2 Nanocomposite

3.1 Introduction

Hybrid materials are a category of materials with unique physical and chemical properties. In the last two decades, there were new developments of hybrid materials such as metal oxide frameworks and nanocomposites. Nanocomposites are usually a class of materials with multi-phases, frequently with one phase dispersed in another phase as the "filler" and the matrix. Hybrid nanocomposites have various applications in bioactivity, optical device and catalysis. [1] Typically, the hybrid nanocomposites are synthesized by the simple mixing technique which results in a heterogeneous dispersion of the fillers. Nanocomposites made in this manner consequently have non-uniform properties.

Hybrid nanocomposites usually exhibit the combined or even enhanced merits from all mixed components. At a structural level, a component can cause distortions in the lattice of the matrix and create structural defects leading to various novel properties. The lattice of the oxide host can also provide the "fillers" with special coordination and bonding environment so as to tune their electronic properties and chemical reactivity. Moreover, metal (A)-oxygen-metal (B) interactions in hybrid metal oxides can promote chemistry not seen in each individual metal oxide component. [2] For example, the silica-based nanocomposites containing superparamagnetic iron oxide nanoparticles (SPIONs), including Fe_3O_4 and γ-Fe_2O_3, are useful for a variety of biological separation and environmental applications such as the removal of contaminants from water. [3] The chemically inert silica serves as a protective layer for the magnetic component and makes

it biocompatible. In addition, the surface silanol groups provide potentials to derivatize and extend the structure with various functional groups. In turn, the iron species endow a magnetic flavor to the plain silica lattice. The synthesis and design of catalysts composed of multiple components has become a hot new research topic. [4-6]

Titanium dioxide (TiO_2) nanomaterials are known for their unusually high photocatalytic properties and other properties such as high density of oxygen vacancies.[7-9] It has been studied and used as a catalyst in various areas such as photocatalysis and oxidation of organic compounds. For example, the commercial product Degussa P25 is commonly selected as the titanium oxide precursor due to its availability and well-characterized physical and chemical properties. Anatase titania is regarded as the photoactive phase of titanium dioxide. Another phase of TiO_2, rutile, generally exhibits lower photocatalytic activity. Rutile phase is the thermodynamically stable form of TiO_2 under ambient conditions. It has been recognized that P25, which is composed of mixed phase of TiO_2 (anatase/rutile with 80/20 in molar ratio), has much higher photocatalytic activities than either pure anatase or rutile phase. [8] The interaction between the two phases at the interface is believed to be the source of increased photocatalytic activity. However, the large band gap (3.2 eV) of titanium oxide still limits its photocatalytic applications because it is only active under the UV wavelength. This has prompted many recent researches to modify the band gap of TiO_2 nanomaterials by doping with different cations and anions, including Ce^{3+}, Mg^{2+} and N^{3-}. [8, 10-14]

Rare earth metal oxides, for example, cerium oxide (CeO_x, x=1.5-2), have also been studied intensively as oxidative catalysts due to their multiple oxidation states and

high oxygen capacity. Cerium oxide, which is usually non-stoichiometric due to the ease of addition and removal of oxygen ions in the oxide lattice, has been considered as an oxygen reservoir in a number of applications including traditional catalytic converters. Previous studies have shown that due to the unique oxygen donating and accepting ability of ceria, it can amorphize some oxides such as titania. Because of the oxygen donating and accepting nature of ceria, there are many oxygen vacancy sites created on the surface of the material. Due to the different crystal structure of ceria (cubic) and titania (tetragonal), the ceria decoration on titania surface is expected to amorphize on the top of titania surface. [11, 15-18] In this work, the structural and catalytic properties of CeO_x-TiO_2 hybrid (CTO) nanocomposite materials were studied. The CTO nanocomposite materials were not only a potential oxidative catalyst but also a new type of nanocomposite materials leading to the new discovery of hybrid materials. Also, by studying this type of material, the understanding of hybrid material will be strengthened and other hybrid materials can be designed according to similar theory.

The dispersion-precipitation method was designed to synthesize the CTO nanocomposites with aims to produce uniform nanoparticle catalyst with high oxidative catalytic activity. In this method, cerium oxide is precipitated on P25 titanium oxide particles dispersed in solution. The oxidation catalytic properties were compared between the CTO nanocomposites.

3.2 Modification of TiO_2 Nanoparticles by the Dispersion–Precipitation Method

Degussa P25 nanoparticles were used as the matrix for the cerium oxide deposition because of their availability. In this method, 0.8 gram of P25 titanium oxide

nanoparticles (AEROXIDE P25, TiO_2, Batch NO. 4168083098, Nippon AEROSIC CO., LTD) was first added into 20 mL of water with vigorous stirring in a 100 mL round bottom flask for 30 min. After the P25 particles were dispersed evenly, 20 mL of the calculated amount of cerium (III) sulfate [$Ce_2(SO_4)_3$] solution was added into the solution. The pH of the mixture was adjusted by NaOH (1M) and HCl (1M). In order to determine the effect of the pH during the synthetic process, a series of reaction mixtures with pH from 1 to 14 was performed during the synthesis. Also, the ceria atomic percentage in the hybrid material was varied from 0.1 at.% to 50 at.% [at.%= Ce atoms/(Ce atoms + Ti atoms)]. The mixture was aged at 25 °C for 15 hours. Afterwards, the sample was filtered using 0.8 μm membranes and rinsed with 400 mL water until the final pH reached about 6. The as-synthesized samples were then heated at 50 °C for 5 hours to drive off the water inside the samples.

The catalysts were activated prior to the catalytic tests as follows, 150 mg of the as-synthesized sample was heated in a 1 inch quartz tube furnace at 450 °C for 1 hour at a pressure of 1 Torr under a 100 standard cubic centimeters per minute (SCCM) of simulated air (20% O_2 and 80% N_2).

3.3 Materials Characterization

X-ray diffraction (XRD) and transmission electron microscopy (TEM) were applied to determine the crystal structure of the synthesized ceira-modified-P25 nanocomposite (CeO_x-P25) samples. The results from the XRD and TEM of the materials synthesized from the dispersion-precipitation method had high consistence and uniformity.

From the XRD patterns in figure 3.1 of the 1 at.% CeO_x-P25 synthesized at various pH levels, the mixed phase of anatase (00-021-1272) and rutile (00-02101276) could be indexed according to JCPDS data. Nonetheless, the ceria content in this case was lower than the detection limit of XRD. So we did not observe peaks belonging to cerium oxide in the XRD pattern. From the peaks' locations in the XRD patterns, the materials synthesized through this method kept the crystal structure of P25 which was a mixture of anatase and rutile with molar ratio of about 80/20. The peaks' locations were not shifted according to the JCPDS data which implied that the lattice structure change could not be detected with the 1 at.% ceria decoration.

From Scherrer's formula

$$t = \frac{0.9\lambda}{B\cos\theta_B}$$

the sizes of the nanocrystallites could be estimated. In this formula, λ is the X-ray wavelength (1.54 Å), B is the full-width at half maximum intensity (FWHM) and θ_B is half of the diffraction angle $2\theta_B$. From the XRD patterns of samples synthesized at varied pH, the FWHM of the anatase (101) peak were about 0.0074 (in radians) which can be referred to a crystallite size of 18.2 nm. The crystallite size was close to the P25 nanoparticle size which suggests that the P25 titanium oxide lattice structure was not affected much by the ceria deposition modification in our synthetic process.

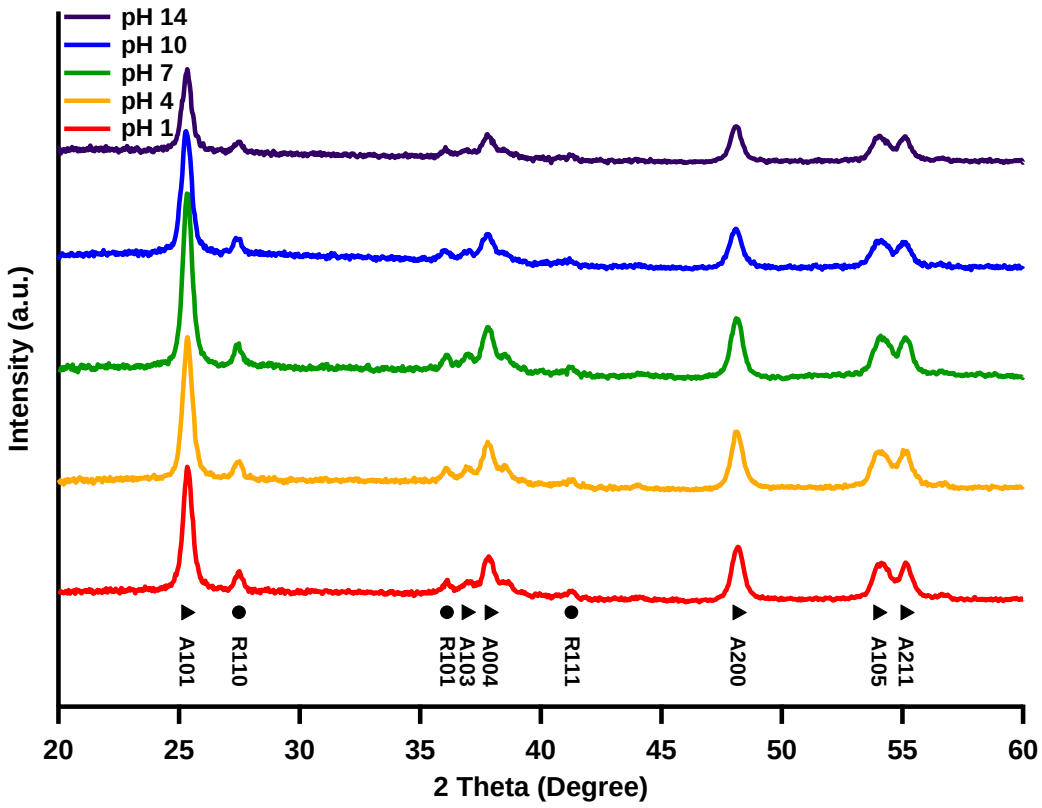

Figure 3.1 XRD patterns of 1 at.% CeO_x-P25 suggested that the structure of P25 was maintained after the dispersion-precipitation of cerium oxide. No significant change in the crystal structures of the samples made at different pHs could be detected. Diffraction peaks were labeled as ▲A: anatase and ●R: rutile.

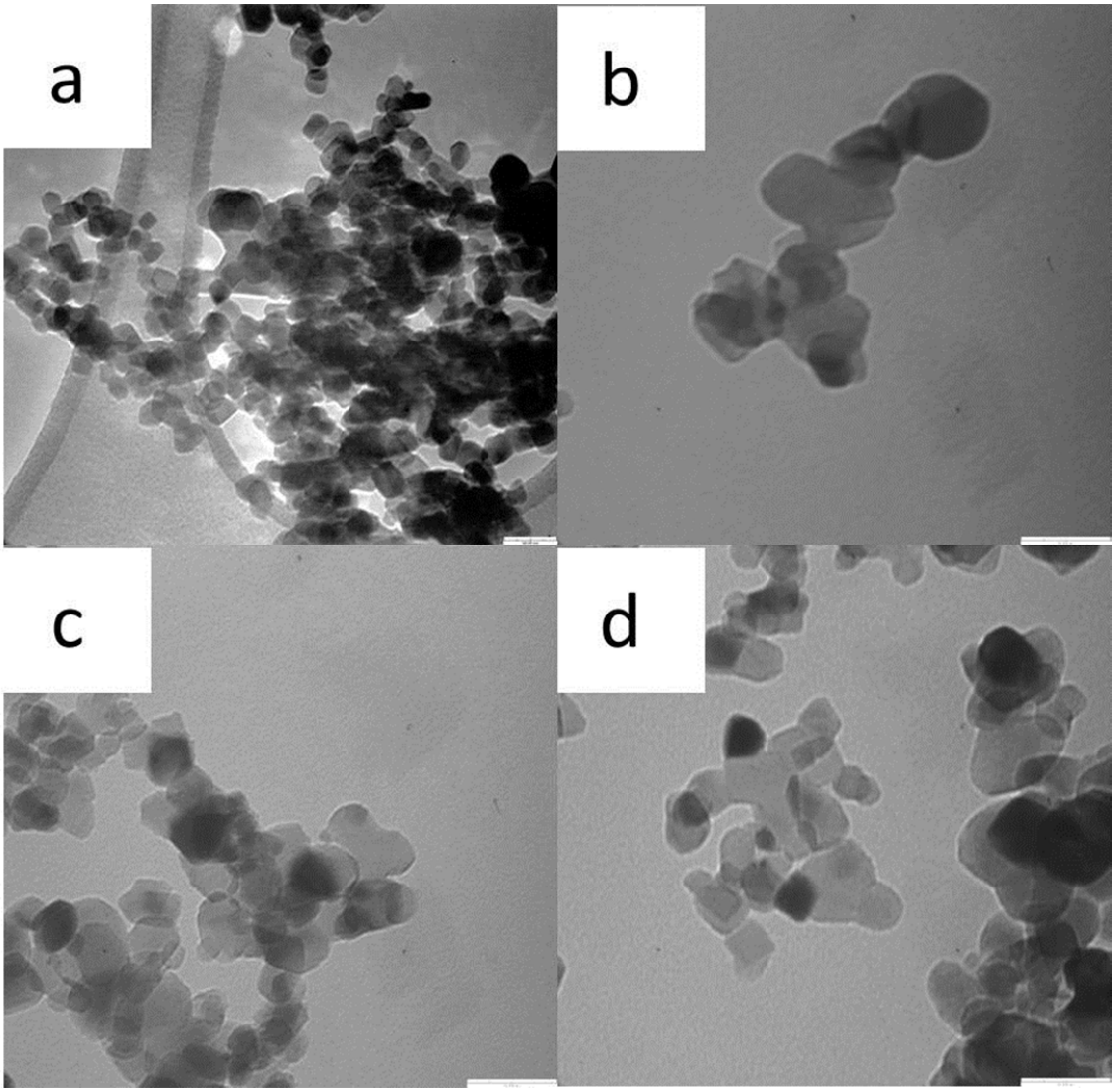

Figure 3.2 TEM images of CeO_x-P25 nanoparticles synthesized using the dispersion-precipitation method. a) pure P25; b) 1 at.% CeO_x-P25 synthesized at pH 7; c) 1 at.% CeO_x-P25 synthesized at pH 14 and d) 1 at.% CeO_x-P25 synthesized at pH 1. All the samples are activated in simulated air at 400 ºC under 1 Torr. The scale bars in all the images are 50 nm.

TEM images, shown in figure 3.2 of the 1 at.% CeOx-P25 samples implied that neither the acidic synthetic condition nor the basic synthetic condition affected the morphology of the P25 particles in these hybrid nanocomposite materials. The only detectable change from the TEM image was the increase in particle diameter after the dispersion-precipitation process. This indicated that the modification by the cerium oxide might had changed the P25 structure but such changes were not significant that to be detected by XRD.

With an increase in the ceria content, the XRD diffraction patterns of the synthesized CeO_x-P25 material changed from that of a mixed phase of anatase and rutile (typical P25) to a fluorite structure which matched the structure of cerium (IV) oxide. From the trend of the crystal structure evolution, the effect of the ceria modification could be inferred to decrease the crystallinity of the TiO_2. For the samples with ceria content from 0.1 at.% to 5 at.%, there were few CeO_2 peaks detected in the corresponding XRD patterns (figure 3.3). However when the ceria percentage was greater than or equal to 10 at.%, the intensities of the CeO_2 peaks increased and the intensities of anatase and rutile peaks decreased. Also, the positions of the anatase peaks did not shift according to the JCPDS data, suggesting the increase of ceria percentage did not introduce the CeO_x into the TiO_2 lattice by XRD. Nonetheless, from the Scherrer's formula, the crystallite size of these samples (table 3.1) increased from 19 nm to 25 nm when ceria percentage increased from 0.1 at.% to 50 at.%. By applying the Scherrer's formula to cerium oxide peaks, the cerium oxide crystallite size (table 3.1) was also found to increase when the ceria percentage increased from 10 at.% to 50 at.% from 7 nm to 13 nm.

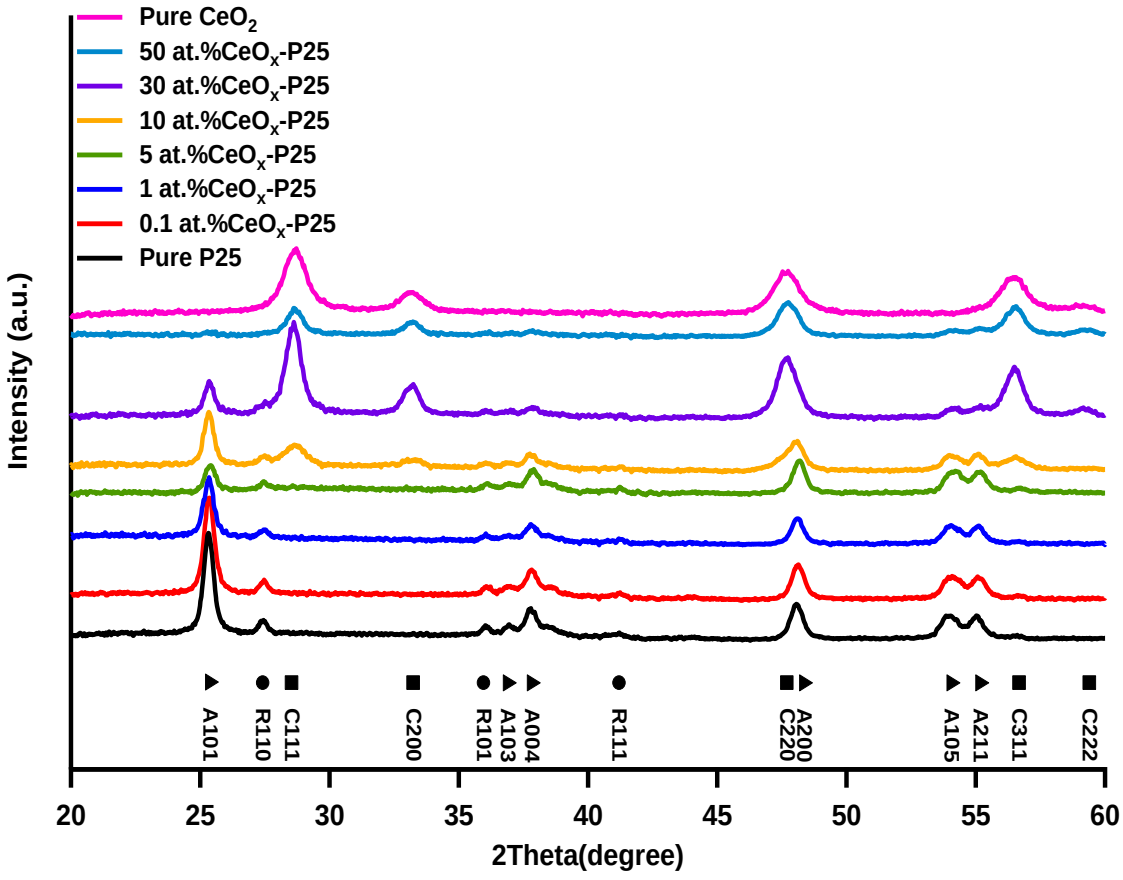

Figure 3.3 XRD patterns of CeO_x-P25 with varied ceria content. From the 0.1 at.% CeO_x to 1/1 Ce/Ti ratio, the crystal structure of the material changed from the mixture of anatase and rutile (P25) to the fluorite cerium oxide structure. The diffraction peaks were labeled as ▲A: anatase, ●R: rutile, ■C: cerium (IV) oxide.

Table 3.1 Anatase Crystallite Size and Ceria Crystallite Size

Sample	Anatase Crystallite Size (nm)		Ceria Crystallite Size (nm)	
	Anatase (101)	Average	Ceria (111)	Average
P25	18.5	16.9	-	-
0.1 at.% CeO_x-P25	19.1	17.0	-	-
1 at.% CeO_x-P25	19.1	18.3	-	-
5 at.% CeO_x-P25	20.1	18.6	-	-
10 at.% CeO_x-P25	20.8	19.5	4.5	5.9
30 at.% CeO_x-P25	20.4	19.6	13.2	10.1
50 at.% CeO_x-P25	25.2	20.0	12.8	10.3
CeO_2	-	-	7.6	6.9

The selected anatase (101) peak and cerium oxide (111) peak were both the most intense peaks in each of the XRD patterns. The average size of the nanocrystallites was estimated from the diffraction peaks between 20° to 60°. The size of the nanocrystallites was estimated using the Scherrer's formula and the full-width at half maximum intensity (FWHM) and θ_B was from the Gaussian fitting of the diffraction peaks.

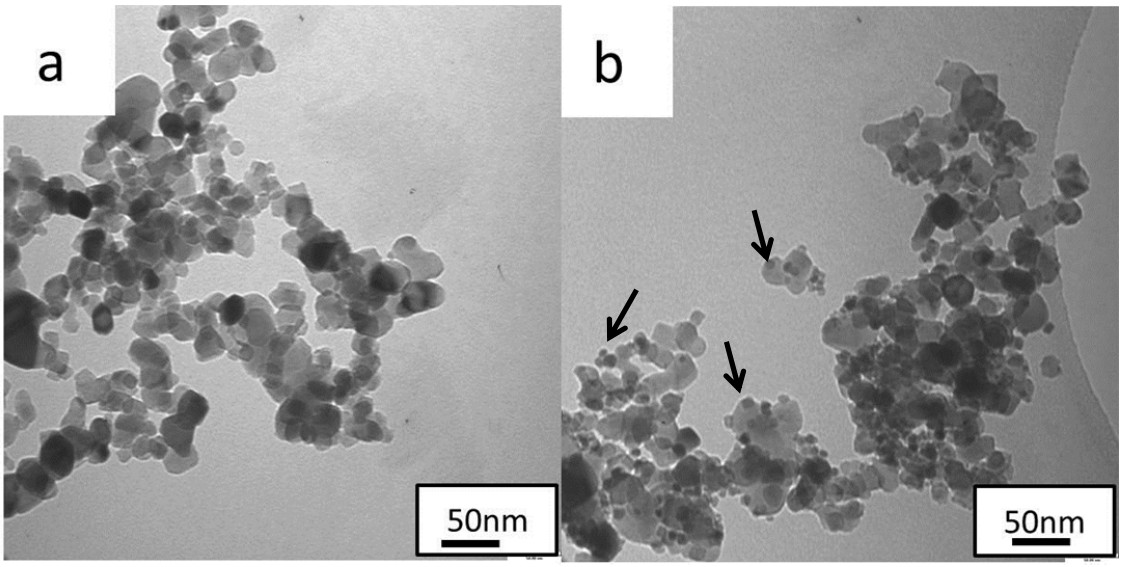

Figure 3.4 TEM images of CeO_x-P25 nanoparticles with different ceria content synthesized from the dispersion-precipitation method. (a) 1 at.% CeO_x-P25 synthesized at pH 14 and (b) 10 at.% CeO_x-P25 synthesized at pH 14. All of these samples were activated in simulated air at 400 SCCM at 1 Torr. Arrows are showing the possible cerium oxide particles.

The TEM image of the 10 at.% CeO_x-P25 sample showed a significant change from the 1 at.% CeO_x-P25 sample with the appearance of the small particles with an average diameter of 8 nm (Figure 3.4). From the image of the 10 at.% CeO_x-P25 sample, small particles were found decorating larger particles. These small particles may be cerium oxide particles.

3.4 Catalysts Evaluation Using Carbon Monoxide Oxidation

The oxidative catalytic activity of the synthesized catalysts was evaluated using the carbon monoxide (CO) oxidation test reactions carried out in a home-built quartz U-tube reactor. The catalysts were set on coarse-grained quartz frit sample platform fixed in one of the branch of the quartz U-tube (Figure 3.5). The precursor gas mixture was composed of 1 vol.% CO, 20 vol.% O_2 and 79 vol.% He. The reactant gas flow was controlled by a mass flow controller at a flow rate of 30 SCCM during the reaction. The eluent of the reaction products was analyzed by gas chromatography (GC) (Agilent 7820A, Santa Clara, CA) equipped with a thermal conductivity detector (TCD). The reactor was heated in a vertical tube furnace. The furnace can control the reaction temperature from room temperature to 500 $^{\circ}$C.

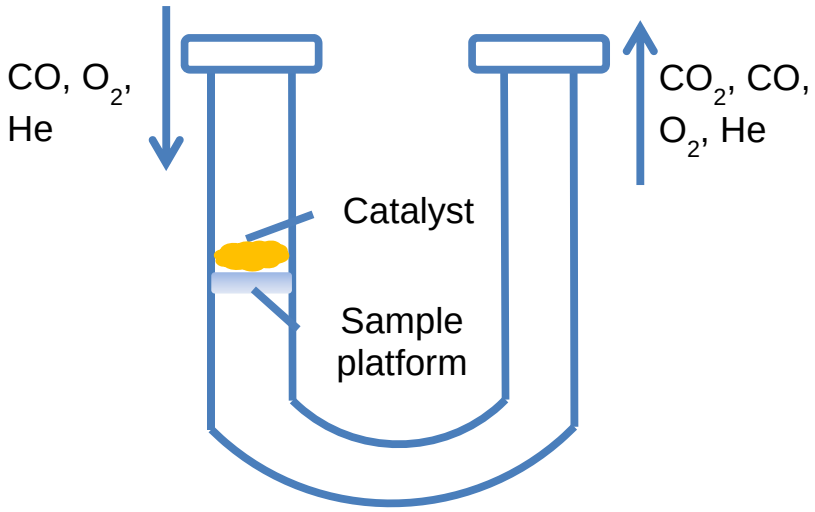

Figure 3.5 Schematic of the U-tube reaction system.

During a typical catalysis test, the reactant gas mixture containing 1 % CO was flowed continuously through the reactor. 100 mg of catalyst was used in each catalysis test. The overall empirical reaction is given by this equation:

$$CO\,(g) + \tfrac{1}{2}\,O_2\,(g) \rightarrow CO_2\,(g)$$

The percentage of CO conversion was determined by analyzing the concentration of reaction product CO_2 in the He carrier gas.

3.4.1 Oxidative catalytic activity of CeO_x-P25 catalyst synthesized at different pH

The oxidative catalytic activity of CeO_x-P25 catalyst made by the dispersion-precipitation method under different pH conditions was evaluated using the CO oxidation bench mark test. A series of 1 at.% CeO_x-P25 samples was synthesized at varied pH as described in section 3.3. Their catalytic activity was determined at a fixed temperature of 200 $^{\circ}$C for 1 hour using the conditions described in section 3.4. The percentage of CO conversion vs. time curve was plotted in figure 3.6. It took about 15 minutes to reach the adsorption-desorption equilibrium at the surface of the catalyst. The percentage of CO conversion was decreasing in the first 15 minutes of the reaction. After the first 15 minutes of reaction, the % of CO conversion became stable. The decrease in the % of CO conversion in the first 15 minutes suggested strong interactions between the reaction gases and the catalyst surface. The catalytic reaction experienced absorption-desorption process. The reaction gas was first absorbed by the catalyst and reacted at the active sites of the catalysts. Some of the active sites possibly lost their activity after the reaction started. In this scenario, the percentage CO conversion would decrease in the first 15 minutes of the reaction and became stable afterwards.

After the first 15 minutes of the reaction, the catalyst synthesized at pH 14 showed a higher CO conversion rate than others made under lower pH conditions. The sample synthesized at pH 14 maintained about 13 % CO conversion. The samples synthesized at pH 4 and pH 1 showed CO conversion percentage lower than 5 %. The CO conversion percentage decreased with the decrease of pH conditions in the synthesis. In general, the catalysts synthesized under basic conditions had higher oxidative catalytic activity under the reaction condition. This could be explained by the reaction taken place during the synthetic process. Cerium (III) sulfates first hydrolyzed in water to form cerium (III) hydroxide [$Ce(OH)_3$]. The $Ce(OH)_3$ was then oxidized both in the drying process and the activation process to form cerium (IV) oxide. During this procedure, the titanium oxide surface was also modified by the hydroxide group under basic conditions or hydronium under acidic conditions. The surfaces that contained higher density of hydroxide groups were expected to have higher affinity to the cerium (III) ions which promote their bonding to the P25 titanium oxide surfaces. It can be inferred that the samples synthesized under basic conditions had higher cerium oxide content anchored onto the surface of P25 according to the CO oxidation catalytic test. In this case, since the CeO_x-P25 synthesized under basic condition had a high catalytic activity, it is better to prepare the CeO_x-P25 in a basic condition to produce catalysts with higher oxidative catalytic activity for CO oxidation.

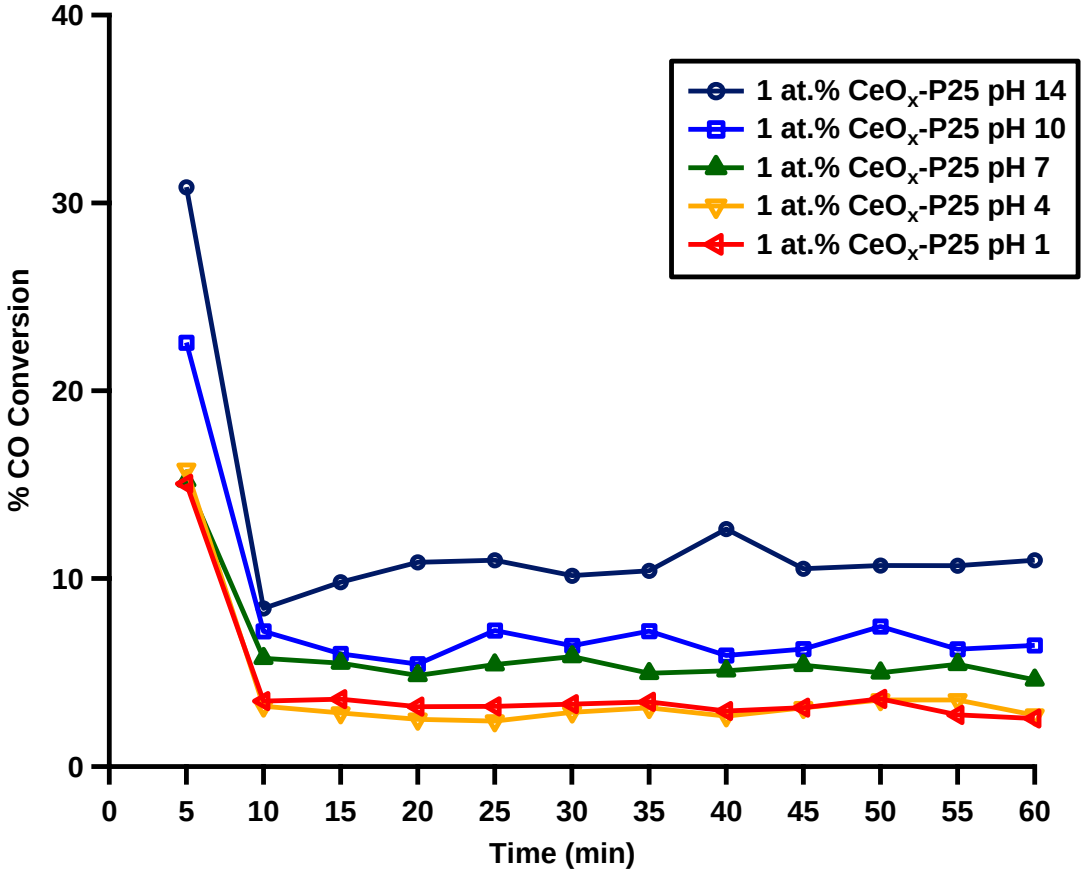

Figure 3.6 Percentage of CO conversion vs. reaction time. The catalytic activity of 1 at.% CeO_x-P25 catalysts prepared under different pH reaction conditions was compared at 200 °C for 1 hour.

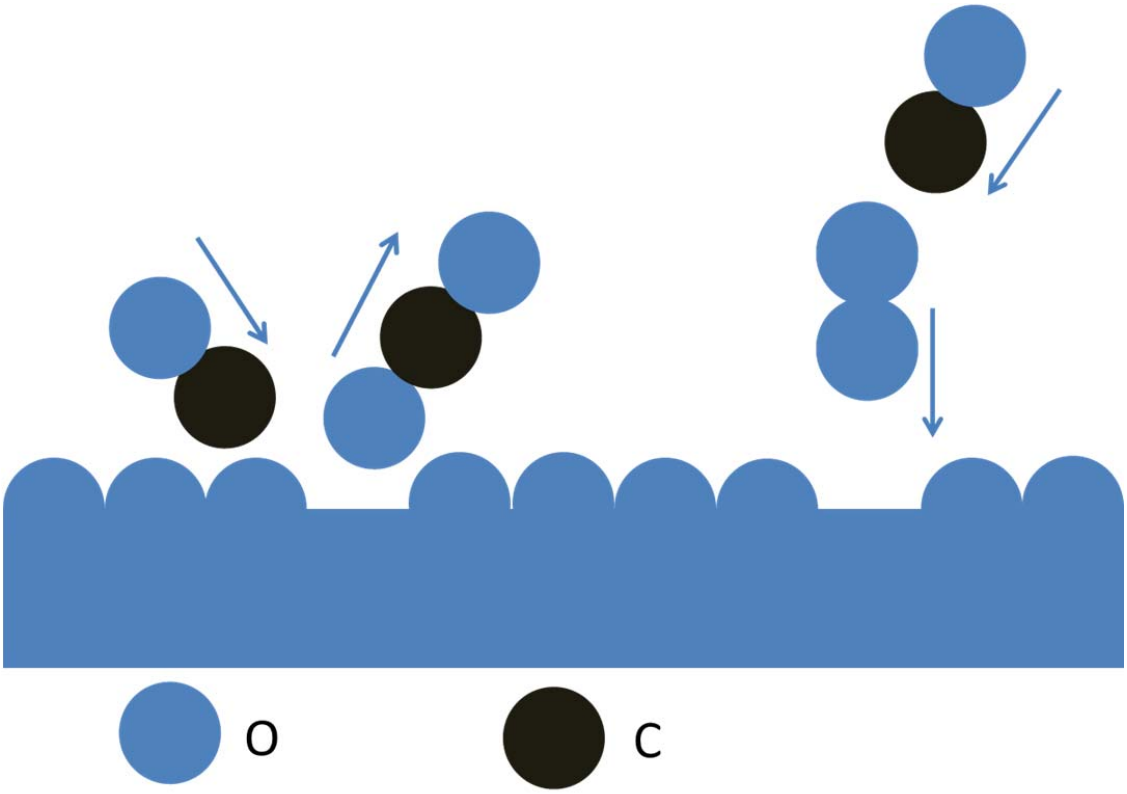

Figure 3.7 Proposed mechanism of CO oxidation on CeO_x-P25 catalyst.

3.4.2 Oxidative catalytic activity of CeO_x-P25 catalyst with varied CeO_x content

The catalytic activity of the CeO_x-P25 also depends on the different amount of ceria content in the catalyst. The catalytic activity was tested over the CeO_x-P25 catalysts with different ceria content. The catalytic test was performed as described in the previous section. The reaction temperature was first increased from 22 °C (room temperature) to 360 °C at 30 °C interval. When the percentage conversion of CO for the tested catalyst is close to 50 %, the reaction temperature increase was every 10 °C in order to obtain a detailed reaction kinetic curve. The catalyst evaluation was stopped after 60 °C past the 100 % CO conversion temperature. All the data points were collected after 1 hour after the mixed gas flowed in order to reach the adsorption-desorption equilibrium at the catalyst surface. Graphs of percentage of CO conversion vs. reaction temperature for catalysts with different ceria content were plotted as figure 3.8.

T_{50} is the temperature at which 50 % of the reactants are converted to the products under a fixed concentration and flow rate of the reactants. It can be applied as a measure of activation energy change by the catalyst and is usually used to evaluate the catalytic activity of a catalyst. Apparent activation energy (E_a) of the CO oxidation reaction can be estimated by the Arrhenius Equation:

$$k(T) = Ae^{-\frac{E_a}{RT}} \text{ or } \ln(k(T)) = \mathrm{C} + (-\frac{E_a}{R})\frac{1}{T}$$

where *k(T)* is the reaction rate, *R* is the ideal gas constant, *T* is the reaction temperature and *A* and *C* are constants for a given reaction conditions.

From figure 3.8, the 5 at.% CeO_x-P25 sample had the lowest T_{50} at 155 °C. As the cerium oxide content in the series of CeO_x-P25 catalysts increased from 0.1 at.% 5 at.%, the corresponding T_{50} of the catalyst dropped from 245 °C to about 155 °C.

However, from the 10 at.% to 50 at.% CeO_x-P25, the corresponding T_{50} of the catalysts started to increase. The T_{50} of 50 at.% CeO_x-P25 was 245 °C which was close to the T_{50} of cerium oxide nanoparticles.

Table 3.2 T_{50} and E_a of CeO_x-P25 with Different CeO_x Content

Sample	T_{50} (°C)	E_a (kJ/mol)
P25	-	-
0.1 at.% CeO_x-P25	240	43.2
1 at.% CeO_x-P25	230	37.3
5 at.% CeO_x-P25	155	29.9
10 at.% CeO_x-P25	230	39.9
30 at.% CeO_x-P25	250	41.2
50 at.% CeO_x-P25	245	41.5
CeO_2	245	38.8

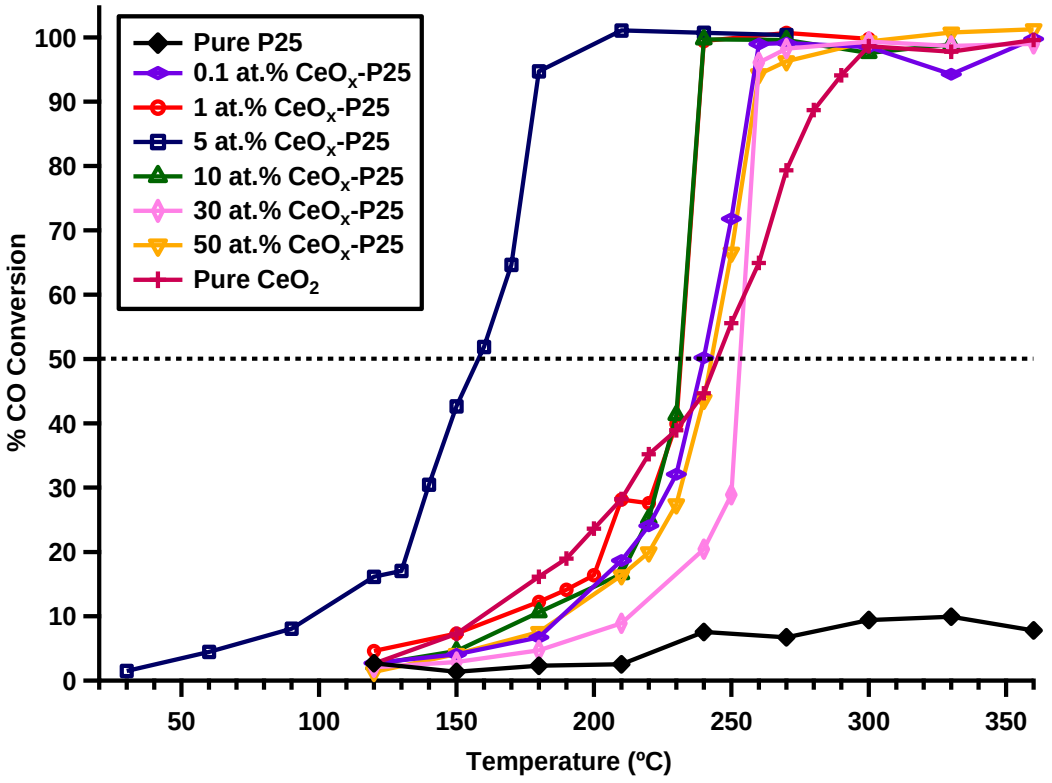

Figure 3.8 Comparison of CO oxidation catalytic activity of CeO_x-P25 catalysts with varied ceria content.

The apparent activation energy (E_a) of the CeO_x-P25 catalyst also depended on the ceria content in the catalysts. Similar to the change of T_{50}, when the cerium content increased from 0.1 at.% to 5 at.%, the E_a decreased, indicating the catalytic activity was increased with the ceria content. While the ceria content increased from 10 at.% to 50 at.%, the E_a increased indicating the catalytic activity decreased.

The change of T_{50} and E_a with the increased content of ceria in the CeO_x-P25 catalyst can possibly be explained with the role of ceria in the series of materials. From the XRD result, all the anatase (101) peak positions did not have significant shift from reported values. This indicated that the deposited ceria did not modify the titanium oxide lattice much, possibly only bonded to the surface of the titanium oxide particles. As the ceria content was increased to 10 at.% and higher, the XRD patterns showed that the diffraction peaks' intensity of cerium oxide increased. When the ceria/titania atomic ratio reached 1:1, the peak intensity of anatase phase became very low in the corresponding XRD patterns and cerium oxide became the major composition of the material. From the TEM images, there was also evidence showing that the 10 at.% CeO_x-P25 was a mixture of titanium oxide nanoparticles and cerium oxide nanoparticles. So with higher ceria content, the cerium oxide became the major composition of the catalyst material. These catalysts had even lower catalytic activity than the 1 at.% CeO_x-P25 possibly because the interaction between the ceria and titania was decreased when "saturated" with ceria.

To verify the effect of the ceria-titania interaction on the surface of the catalyst, a test was performed to compare the catalytic activity of the CeO_x-P25 nanocomposite catalyst and a catalyst composed of a mixture of CeO_x and P25 particles. From Figure 3.9,

the difference between the T_{50}'s could be an evidence of the ceria-titania interaction which may explain the increase in the catalytic activity of the CeO_x-P25 nanocomposite.

The stability of the catalytic activity of 5 at.% CeO_x-P25 nanocomposite was evaluated with a 20-h.-long CO oxidation test at 150 °C. The percentage of CO conversion decreased about only 10 % during the test (Figure 3.10), indicating the long term activity of catalysts.

3.5 Conclusion

The dispersion-precipitation method was applied to modify the P25 titanium oxide nanoparticles and develop a new type of ceria-titania hybrid catalyst. Although further more detailed characterization is needed to confirm the structure of the CeO_x-P25 hybrid nanocomposites and understand the catalytic mechanism of the hybrid oxide catalyst, the currently demonstrated catalytic results and the structural characterization indicated that as the ceria content of CeO_x-P25 increased from 0 to 5 at.%, the catalytic activity increased and the apparent structure of titanium oxide remained intact.

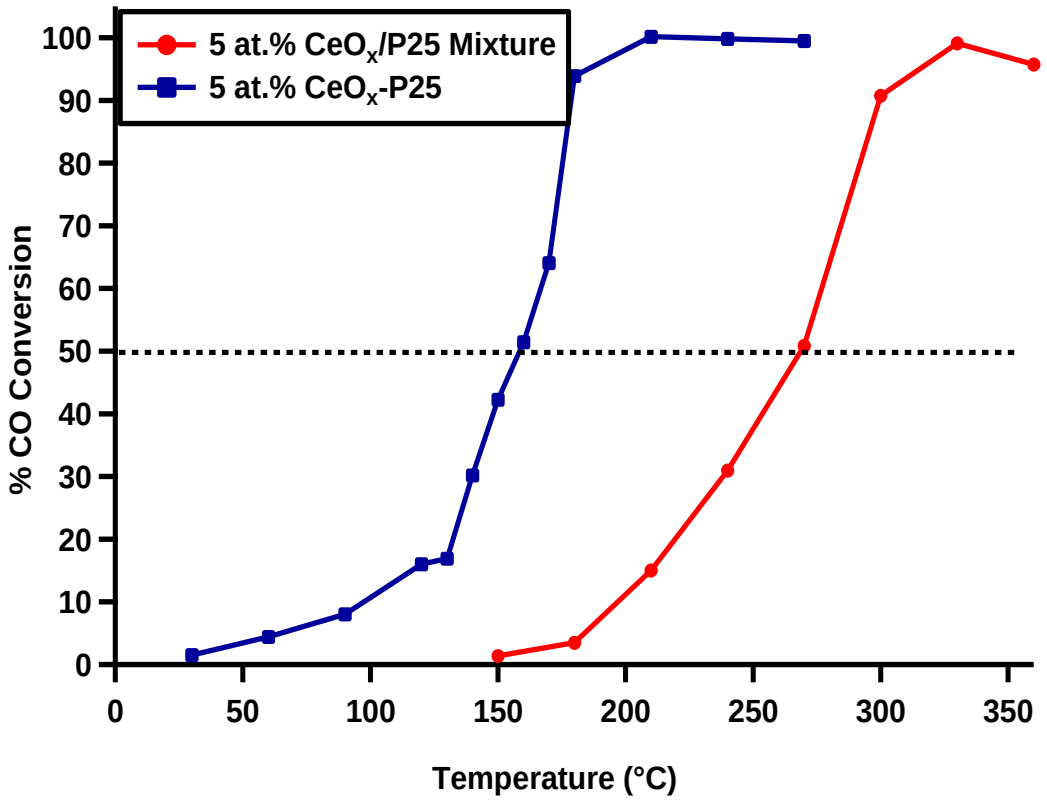

Figure 3.9 Comparison of CO oxidation activity of a 5 at.% CeO_x-P25 nanocomposite and a catalyst composed of P25 nanoparticles with 5 at.% bulk ceria.

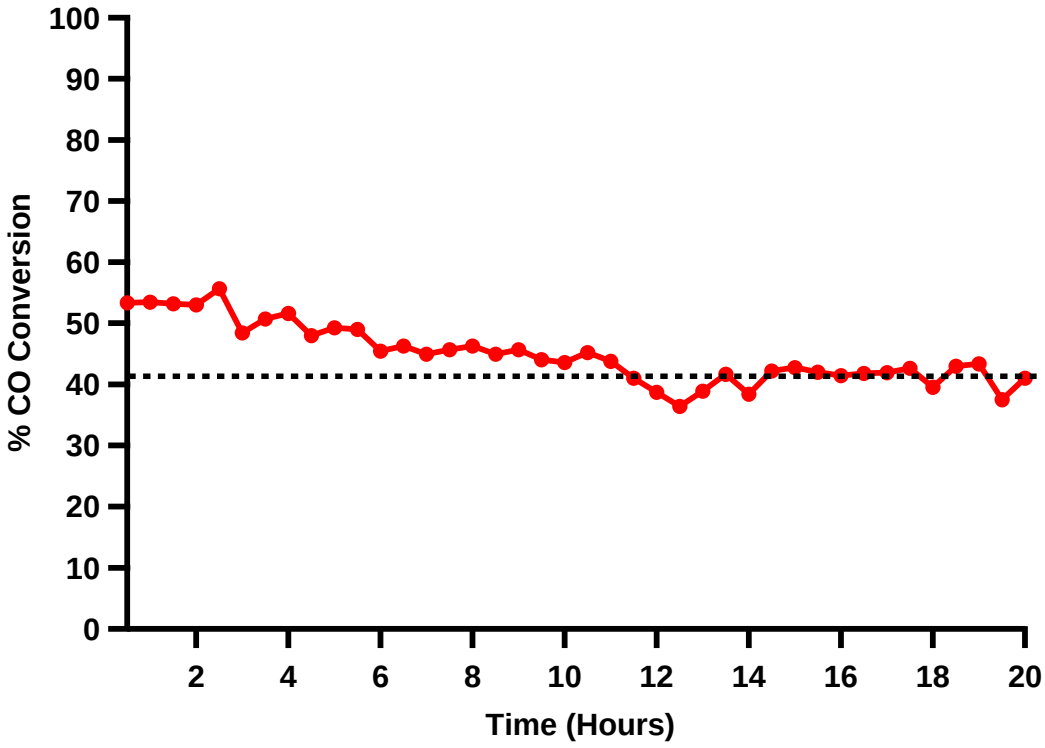

Figure 3.10 The 20-hour-long CO oxidation catalysis test of 5 at.% CeO_x-P25 at 150 ºC.

3.6 References

1. Eder, D., *Carbon Nanotube-Inorganic Hydrids.* Chemical Reviews, 2010. **110**: p. 1348-2385.
2. Di Valentin, C., Diebold, U., and Selloni, A., *Doping and functionalization of photoactive semiconducting metal oxides.* Chemical Physics, 2007. **339**(1-3): p. Vii-Viii.
3. Deng, Y., Qi, D., Deng, C., Zhang, X., and Zhao, D., *Superparamagnetic high-magnetization microspheres with an Fe_3O_4@SiO_2 core and perpendicularly aligned mesoporous SiO_2 shell for removal of microcystins.* Journal of the American Chemical Society, 2008. **130**(1): p. 28-29.
4. Luo, B.M., Yang, H., Liu, S., Fu, W., Sun, P., Yuan, P., Zhang, Y., and Liu, Z., *Fabrication and characterization of self-organized mixed oxide nanotube arrays by electrochemical anodization of Ti-6Al-4V alloy.* Materials Letters, 2008. **62**(30): p. 4512-4515.
5. Mor, G.K., Prakasam, H.E., Varghese, O.K., Shankar, K. and Grimes, C.A., *Vertically oriented Ti-Fe-O nanotube array films: Toward a useful material architecture for solar spectrum water photoelectrolysis.* Nano Letters, 2007. **7**(8): p. 2356-2364.
6. Wilkening, M., Lyness, C., Armstrong, A.R., and Bruce, P.G., *Diffusion in Confined Dimensions: Li^+ Transport in Mixed Conducting TiO_2-B Nanowires.* Journal of Physical Chemistry C, 2009. **113**(12): p. 4741-4744.

7. Kontos, A.I., Likodimos, K.V. Stergiopoulos, T., Tsoukleris, D.S., and Falaras, P., *Self-Organized Anodic TiO_2 Nanotube Arrays Functionalized by Iron Oxide Nanoparticles.* Chemistry of Materials, 2009. **21**(4): p. 662-672.

8. Keller, V., Bernhardt, P., and Garin, F., *Photocatalytic oxidation of butyl acetate in vapor phase on TiO_2, Pt/TiO_2 and WO_3/TiO_2 catalysts.* Journal of Catalysis, 2003. **215**(1): p. 129-138.

9. Matsuoka, Y., and Matsuoka, O., *Chain Structures of Surface Hydroxyl Groups Formed via Line Oxygen Vacancies on TiO_2 (110) Surfaces Studied Using Noncontact Atomic Force Microscopy.* Journal of Physical Chemistry B, 2005. **109**(50): p. 23948-23954.

10. Fornasiero, P., Dimonte R., Rao G. R., Kaspar J., Meriani S., Trovarelli A. and Graziani M, *Rh-Loaded CeO_2-ZrO_2 Solid-Solutions as Highly Efficient Oxygen Exchangers: Dependence of the Reduction Behavior and the Oxygen Storage Capacity on the Structural-Properties.* Journal of Catalysis, 1995. **151**(1): p. 168-177.

11. Yang, Z.X., He, B., Lu, Z., and Hermansson, K., *Physisorbed, Chemisorbed, and Oxidized CO on Highly Active Cu-CeO_2(111).* Journal of Physical Chemistry C, 2010. **114**(10): p. 4486-4494.

12. Gluhoi, A.C., Dekkers, M.A.P., and Nieuwenhuys, B.E., *Comparative studies of the N_2O/H_2, N_2O/CO, H_2/O_2 and CO/O_2 reactions on supported gold catalysts: effect of the addition of various oxides.* Journal of Catalysis, 2003. **219**(1): p. 197-205.

13. Murray, E.P., Tsai, T., and Barnett, S.A., *A direct-methane fuel cell with a ceria-based anode.* Nature, 1999. **400**(6745): p. 649-651.

14. Connor, P.A. and McQuillan, A.J., *Phosphate adsorption onto TiO_2 from aqueous solutions: An in situ internal reflection infrared spectroscopic study.* Langmuir, 1999. **15**(8): p. 2916-2921.

15. Paulose, M., Varghese, O.K., Mor, G.K., Grimes, C.A. and Ong, K.G., *Unprecedented ultra-high hydrogen gas sensitivity in undoped titania nanotubes.* Nanotechnology, 2006. **17**(2): p. 398-402.

16. Wang, Q.L., Varghese, O., Grimes, C.A. and Dickey, E.C., *Grain boundary blocking and segregation effects in yttrium-doped polycrystalline titanium dioxide.* Solid State Ionics, 2007. **178**(3-4): p. 187-194.

17. Soo, Y.L., Weng, S.C., Sun, W.H., Chang, S.L., Lee W.C., Chang, Y.S., Kwo, J., and Hong, M., *Local environment surrounding Co in MBE-grown Co-doped HfO_2 thin films probed by EXAFS.* Physical Review B, 2007. **76**(13): p. 132404.

18. Nolan, M., *Molecular Adsorption on the Doped (110) Ceria Surface.* Journal of Physical Chemistry C, 2009. **113**(6): p. 2425-2432.

Chapter 4 Future Work

One of the goals of this thesis is to understand the catalysis of nanostructured rare earth metal oxide catalysts by exploiting the metal oxide and the hybrid metal oxide nanocomposites as working examples. The described hybrid CeO_x-TiO_2 nanocomposites in Chapter 3 is a catalyst with the potential to be applied as a commercial oxidative catalyst because of the low content of rare earth needed in the catalyst. Although catalysts with reduced T_{50} are desirable for saving thermal energy needed for catalytic reaction, there are major issues to consider in designing catalysts for industrial use such as the chemical and thermal stability of the catalysts.

Different methods could induce different crystal structures of the cerium oxide and different interactions between the cerium oxide "filler" and the titanium oxide matrix. The hybrid metal oxide nanocomposites have shown enhanced catalytic behavior for CO oxidation reaction compared to each of the single component. This enhancement is likely due to the small amount (5 at.% as added) of ceria species. The incorporated ceria species may cover the surface of titania nanostructures and form spherical shells of CeO_x with surface oxygen defects depending on the lattice structures of the titania layers underneath it. The titania structure, as the matrix of the sphere, has dual functions as both the support of ceria and oxygen provider to the ceria-rich surface. To fully understand the catalytic mechanism of the hybrid metal oxide catalyst, further study of the hybrid metal oxide catalyst using techniques including high resolution TEM analysis, select area electron diffraction (SAED), Raman scattering spectroscopy, extended X-ray absorption fine structure (EXAFS) is needed for understanding the lattice structure of the hybrid metal

oxide catalyst, the metal-oxygen-metal bond energy and other interactions between the ceria "filler" and the titanium oxide matrix.

4.1 Porous Cerium Oxide Membranes

The effectiveness of the porous structures in cerium oxide nanoporous membranes discussed in Chapter 2 can be evaluated in prototype solid oxide fuel cells. As discussed in Chapter 2, cerium oxide has been used as the electrolyte in the solid oxide fuel cells and the reaction temperature of the cell is usually up to 1000 °C. We expected that SOFCs with nanoporous cerium oxide membranes or the decorated cerium oxide membrane may maintain similar efficiency with lower reaction temperature. Moreover, the highly hydrophobic surface of the nanoporous cerium oxide membrane may further increase the efficiency of the fuel cell because the hydrophobic surface will not be poisoned by the water formed in the fuel cell.

4.2 CeO_x-TiO_2 Nanocomposites

We have found that the CeO_x-TiO_2 nanocomposite (CTO) has shown improved catalytic activity over the cerium oxide or titanium oxide separately. The understanding of the interaction between CeO_x and TiO_2 and the corresponding enhancement mechanism is still lacking. Two methods have been attempted to synthesize the CTO nanocomposite with higher catalytic activity. Preliminary results are discussed as follows.

4.2.1 Modification of TiO_2 nanotubes by dispersion-precipitation method

One way to increase the catalytic activity of the material is to increase the active surface area of the catalyst. [1-4] Titanium oxide nanotubes as a type of materials with

large surface area is considered to replace the P25 titania particles to obtain a CTO hybrid nanocomposite. The dispersion-precipitation method was also applied to synthesize the ceria modified titanium oxide (anatase) nanotubes (CeO_x-ATNT) in order to pursue a catalyst with high catalytic activity. The material was prepared at pH 14 condition with varied ceria content. The titanium oxide nanotubes were prepared from a hydrothermal method. Preliminary characterization and CO oxidation test have been performed to study the CeO_x-ATNT material. [3-6]

4.2.2 Characterization of the ceria modified titanium oxide nanotubes

The CeO_x-ATNT nanocomposites were characterized by XRD. From the XRD patterns in figure 4.1, the 1 at.% CeO_x-ATNT showed typical diffraction peaks for anatase phase without detectable peak shift from the standard anatase XRD pattern. However, by comparing the XRD patterns the signal/noise ratio of the pattern of 1 at.% CeO_x-ATNT was much lower than that of the 1 at.% CeO_x-P25 sample. This suggests that the CeO_x-ATNT sample had lower crystallinity than the CeO_x-P25 sample. The 5 at.% CeO_x-ATNT sample which showed no typical anatase diffraction peaks indicated that the anatase structure was turned into amorphous after the cerium oxide modification. The crystallite size was also estimated by Scherrer's formula. Also, using Scherrer's formula, the crystallite size of the 1 at.% CeO_x-ATNT sample was estimated to be about 18 nm, which was close to that of the 1 at.% CeO_x-P25 sample (Table 4.1).

Table 4.1 Anatase Grain Size of 1 at.% CeO_x-ATNT and CeO_x-P25

Sample	Anatase Crystallite Size (nm)	
	Anatase (101)	Average
P25	18.5	16.9
1 at.% CeO_x-P25	19.1	18.3
1 at.% CeO_x-ATNT	18.1	17.0

The catalytic activity of the ceria decorated titanium oxide nanotubes were also tested using the same method as the one for CeO_x-P25 samples. The T_{50} and the percentage of CO conversion vs. temperature curve of the 1 at.% CeO_x-ATNT were almost same with that of the 1 at.% CeO_x-P25 sample (Figure 4.2). The titanium oxide nanotubes had much higher surface area than the P25 nanoparticles which should increase the catalytic activity. However, the crystallinity of the CeO_x-ATNT was much lower than those of the CeO_x-P25 samples according to the XRD patterns. From the CO oxidation result, it can be inferred that the crystallinity played an important role in the oxidation catalysis. Although the CeO_x-ATNT catalysts have higher surface area, their lower crystallinity limits their catalytic activity.

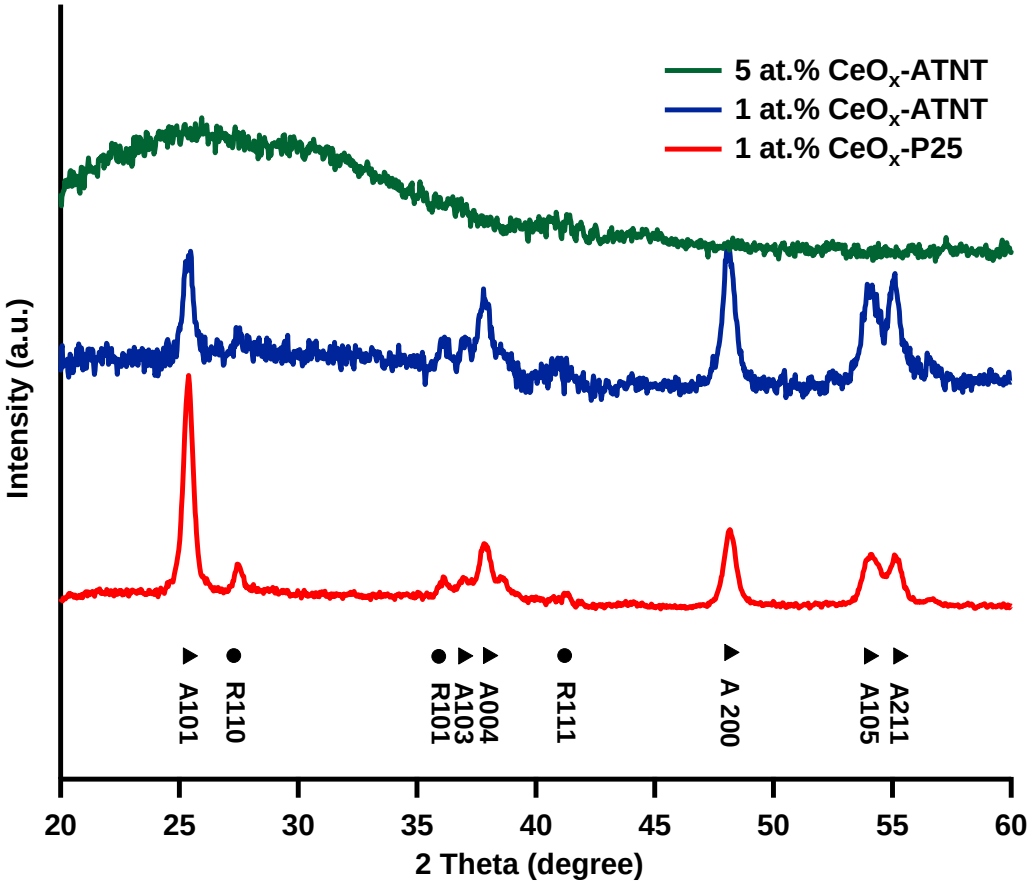

Figure 4.1 XRD patterns of CeO_x-ATNT with 1 at.% ceria and 5 at.% ceria, the crystal structure of the material changed from the anatase phase to amorphous. ▲A: anatase, ●R: rutile.

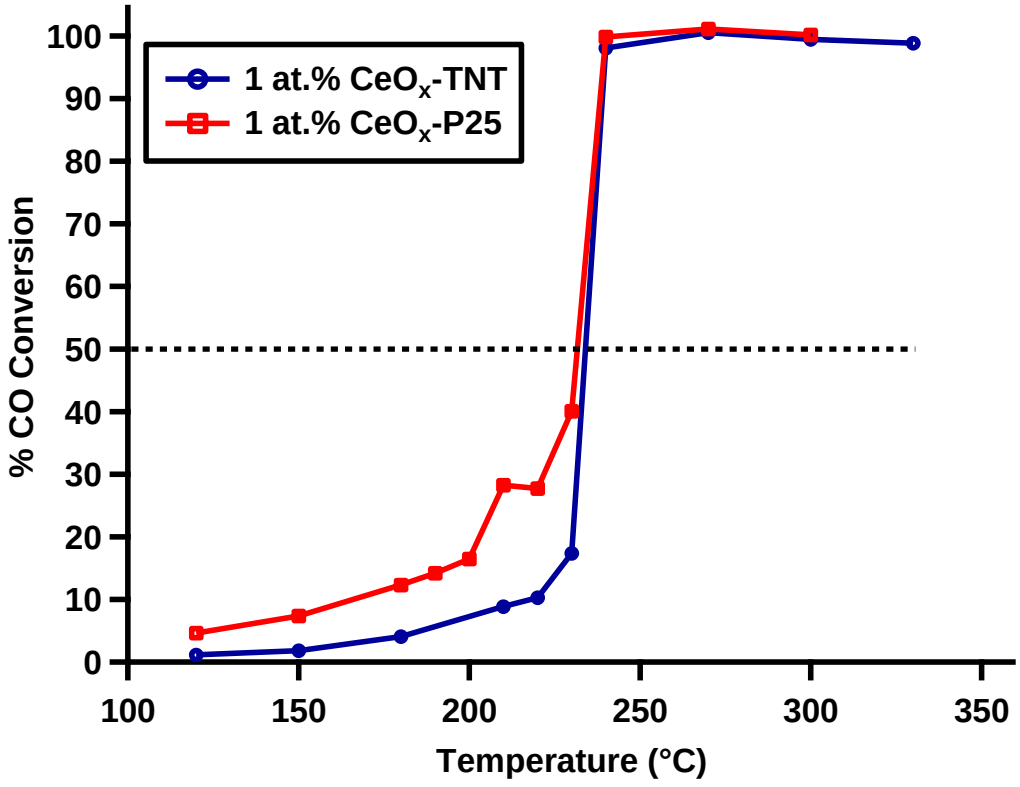

Figure 4.2 Comparison of CO oxidation catalytic activity of 1 at.% CeO_x-ATNT and 1 at.% CeO_x-P25.

4.2.3 One-step synthesis of ceria/titania mixed oxide nanoparticles

A "one-step" synthetic strategy was attempted to produce ceria/titania mixed oxide nanoparticles. A sample of 1.6 gram of titanium oxide sulfate ($TiOSO_4$, Alfa Aesar, Ward Hill, MA) was first added into 20 mL of water with vigorous stirring in a 100 mL round bottom flask for 30 min. until the mixture turned clear which indicated the TiO_2 sol was formed. Afterwards, 20 mL of the calculated amount of $Ce_2(SO_4)_3$ solution was added into the sol. The sol solution finally reached a pH of 2. The sol was aged at 25 °C for 15 hours and then the sol was heated at 80 °C to evaporate the about 40 mL water. The sample was then filtered using 0.8 μm membranes (Millipore, Billerica, MA) and rinsed with 200 mL DI water until the final pH reached 6. After the rinsing step, the as-synthesized samples were heated at 50 °C for 5 hours to drive off the water inside the sample.

The same activation procedure as described in section 3.2 was performed before the catalytic oxidation evaluation of the catalysts.

4.2.4 Characterization of the ceria/titania from "one-step" method

X-ray diffraction (XRD) was applied to determine the crystal structure of the ceria decorated titania (CeO_x/TiO_2) samples from the two different methods. According to the JCPDS data, the XRD pattern of the sample synthesized from the "one-step" method showed that the activation process converted the as synthesized sample from amorphous to a mixture of titanium oxide anatase and rutile structure. However, with the addition of the ceria species, there were also peaks indicating cerium titanate species present in the samples. The cerium titanate peaks were detected in all the samples with different ceria

content. From the 0.1 at.% CeO_x/TiO_2 sample to 1 at.% CeO_x/TiO_2 sample, the intensities and the positions of the peaks changed little but the pattern of 10 at.% CeO_x/TiO_2 sample showed a decrease in signal/noise ratio. This suggested that the addition of ceria decreased the crystallinity of the sample**.**

Most of the diffraction peaks had their positions shifted for all the samples synthesized by this method. According to the Bragg's law:

$$2d \sin\theta = \lambda$$

where d is the adjacent lattice plane spacing, θ is the diffraction angle, λ is the wavelength of the X-ray. The change on the lattice constant could be estimated using this formula. Comparing with the JCPDS data, the two theta diffraction angle of CeO_2 (111) peak increased by 0.9° which indicated that the (111) lattice spacing decreased by 3%. The decrease of the (111) lattice spacing suggested that the titanium atoms might had affected the cerium oxide structure. From the XRD pattern, there were diffraction peaks not belonging to any cerium oxide or titanium oxide species. These peaks may lead to new cerium titanate structure, but more studies are needed to gain a deeper understanding of these structures.

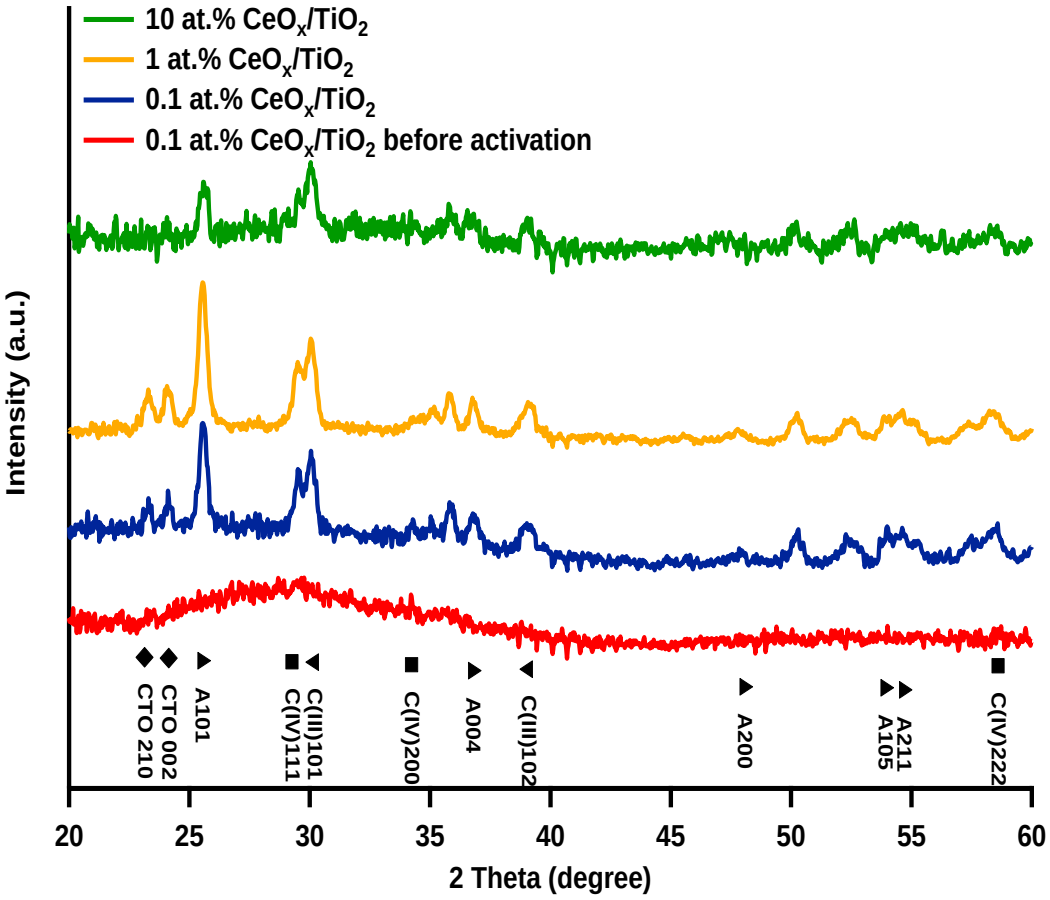

Figure 4.3 XRD patterns showing the structure transformation of the as-synthesized CeO_x/TiO_2 samples to the mixed titanium oxide anatase and rutile with certain amount of cerium titanate. Diffraction peaks were labeled as ▲A: anatase, ■C (IV): cerium (IV) oxide, ▼C (III): cerium (III) oxide and ♦CTO: cerium titanate species.

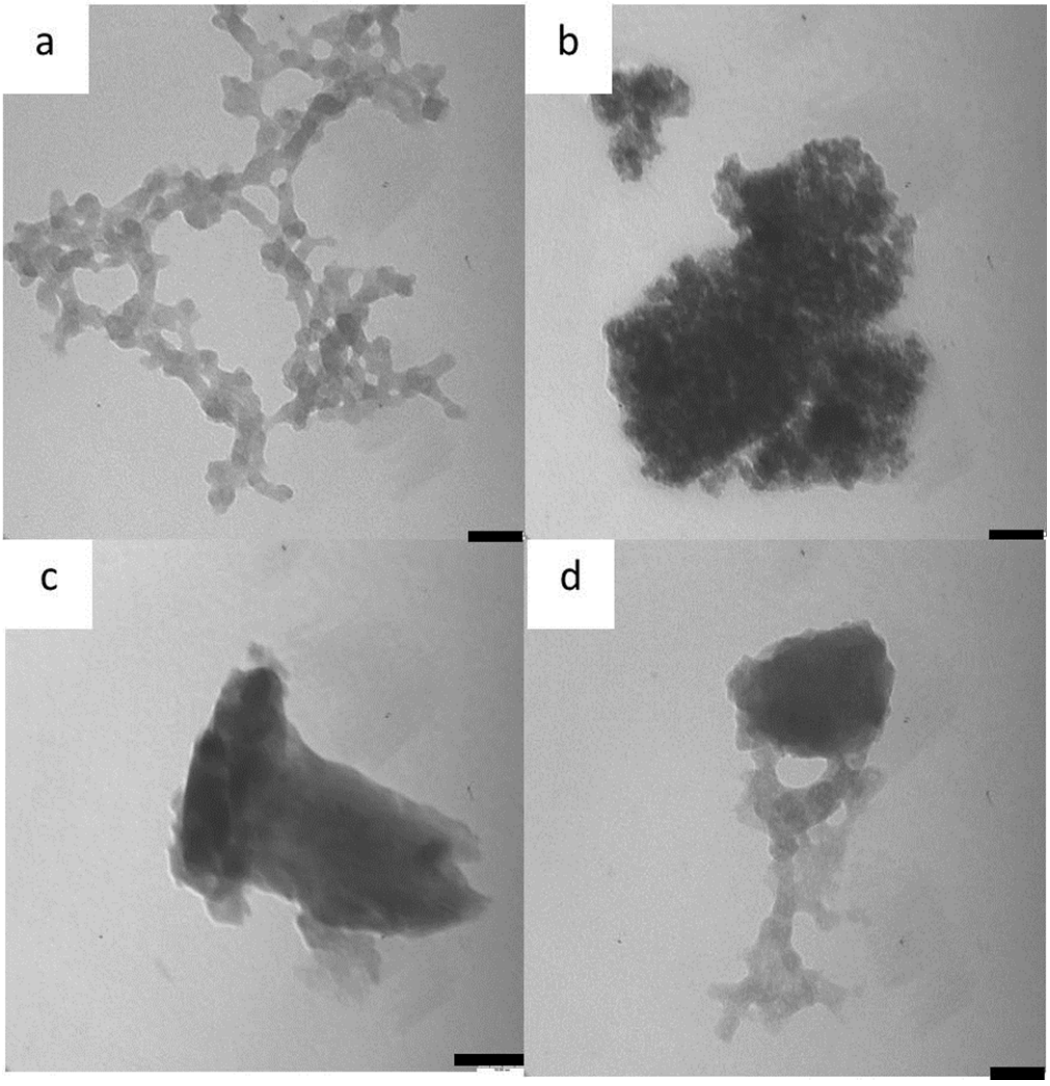

Figure 4.4 TEM images of CeO_x/TiO_2 nanoparticles synthesized from the "one-step" method. (a) 0.1 at.% CeO_x/TiO_2, (b) 1 at.% CeO_x/TiO_2, (c) 10 at.% CeO_x/TiO_2 and (d) TiO_2 without cerium oxide coating. All the samples are after activated. The scale bars in all the images are 50 nm.

From the TEM images of the CeO_x/TiO_2 nanoparticles synthesized using the "one-step" method (Figure 4.4), nanoparticles could be easily identified in the 1 at.% CeO_x/TiO_2 sample but not in the : 0.1 at.% CeO_x/TiO_2 and 10 at.% CeO_x/TiO_2. One possibility was that those particles were agglomerated together in these two samples.

4.3 Future Work Plan

From all the preliminary results, we expect the hybrid nanocomposites to be a group of promising catalysts with high oxidation activity and low rare earth content. Further study is needed to understand the principles of the catalytic process and the hybrid nanocomposite design.

For the "one-step" method, the precursors need to be selected before the synthetic procedures in order to form uniformed catalyst. For the dispersion-precipitation method, the titanium oxide substrates need be further studied and titanium oxide nanotubes with both high crystallinity and surface area will be the desirable substrate. Using the anodization method, titanium oxide nanotube with high surface area and high crystallinity can be fabricated as the titanium oxide substrates for the hybrid composite catalysts. [7-12] Upon further optimization of the synthetic method, the other rare earth metals/metal oxides can be applied to modify the titanium oxide surface to form different hybrid nanocomposites with unique properties. This will lead to a better understanding of the dopants effect on the mechanism of lattice modification and crystal engineering.

Last but not least, the study of noble metal-doped metal oxides nanocomposites will enhance our understanding in the strong metal-support interaction and the exploration of new oxidative catalysts. Studies have shown that both the gold-doped

titanium oxide and gold-doped cerium oxide have improved catalytic activity in reactions such as CO oxidation. Using hybrid oxide composites as substrate supports, the interaction between the noble metal and the support is expected to be much more complex and interesting.

4.4 Summary

The research presented in this thesis focuses on the understanding of the principles behind the synthesis and catalytic properties of the cerium oxide related materials. With further study, the understanding of the role of defects and the catalytic activity of the hybrid nanocomposite will be strengthened. I expect that the present study of the hybrid nanocomposite catalysts may advance the design and engineering of tandem catalyst systems.

4.5 References

1. Pan, C., Zhang, D., Shi, L., and Fang, J., *Template-Free Synthesis, Controlled Conversion, and CO Oxidation Properties of CeO_2 Nanorods, Nanotubes, Nanowires, and Nanocubes.* European Journal of Inorganic Chemistry, 2008. **2008**(15): p. 2429-2436.
2. Chen, G.Z., Xu, C., Song, X., Zhao, W., Ding, Y., and Sun, S., *Interface reaction route to two different kinds of CeO_2 nanotubes.* Inorganic Chemistry, 2008. **47**(2): p. 723-728.
3. Meuer, S., Fischer, K., Mey, I., Janshoff, A., Schmidt, M., and Zentel, R., *Liquid Crystals from Polymer-Functionalized TiO_2 Nanorod Mesogens.* Macromolecules, 2008. **41**(21): p. 7946-7952.
4. Paulose, M., Peng, L., Popat, K.C., Varghese, O.K., LaTempa, T.J., Bao, N., Desai, T.A., and Grimes, C.A., *Fabrication of mechanically robust, large area, polycrystalline nanotubular/porous TiO_2 membranes.* Journal of Membrane Science, 2008. **319**(1-2): p. 199-205.
5. Roy, S.C., Paulose, M., and Grimes, C.A., *The effect of TiO_2 nanotubes in the enhancement of blood clotting for the control of hemorrhage.* Biomaterials, 2007. **28**(31): p. 4667-4672.
6. Yoriya, S., Mor, G.K., Sharma, S., and Grimes, C.A., *Synthesis of ordered arrays of discrete, partially crystalline titania nanotubes by Ti anodization using diethylene glycol electrolytes.* Journal of Materials Chemistry, 2008. **18**(28): p. 3332-3336.

7. Allam, N.K. and Grimes, C.A., *Formation of vertically oriented TiO_2 nanotube arrays using a fluoride free HCl aqueous electrolyte.* Journal of Physical Chemistry C, 2007. **111**(35): p. 13028-13032.

8. Kontos, A.I., Likodimos, V, Stergiopoulos, T., Tsoukleris, D.S. and Falaras, P., *Self-Organized Anodic TiO_2 Nanotube Arrays Functionalized by Iron Oxide Nanoparticles.* Chemistry of Materials, 2009. **21**(4): p. 662-672.

9. Liang, H.C. and Li, X.Z., *Visible-induced photocatalytic reactivity of polymer-sensitized titania nanotube films.* Applied Catalysis B-Environmental, 2009. **86**(1-2): p. 8-17.

10. Mor, G.K., Varghese, M., Paulose, M. and Grimes, C.A., *Transparent highly ordered TiO_2 nanotube arrays via anodization of titanium thin films.* Advanced Functional Materials, 2005. **15**(8): p. 1291-1296.

11. Matthey, D., Wang, J.G., Wendt, S., Matthiesen, J., Schaub, R., Lagsgaard, E., Hammer, B., and Besenbacher, F., *Enhanced bonding of gold nanoparticles on oxidized $TiO_2(110)$.* Science, 2007. **315**(5819): p. 1692-1696.

12. Nijhuis, T.A.R., Visser, T., and Weckhuysen, B.M., *The role of gold in gold-titania epoxidation catalysts.* Angewandte Chemie-International Edition, 2005. **44**(7): p. 1115-1118.